

Observation of unconventional many-body scarring in a quantum simulator

Guo-Xian Su,^{1,2,3} Hui Sun,^{1,2,3} Ana Hudomal,⁴ Jean-Yves Desaulles,⁴ Zhao-Yu Zhou,^{1,2,3}
Bing Yang,⁵ Jad C. Halimeh,⁶ Zhen-Sheng Yuan,^{1,2,3} Zlatko Papić,⁴ and Jian-Wei Pan^{1,2,3}

¹*Hefei National Laboratory for Physical Sciences at Microscale and Department of Modern Physics,
University of Science and Technology of China, Hefei, Anhui 230026, China*

²*Physikalisches Institut, Ruprecht-Karls-Universität Heidelberg,
Im Neuenheimer Feld 226, 69120 Heidelberg, Germany*

³*CAS Center for Excellence and Synergetic Innovation Center in Quantum Information and Quantum Physics,
University of Science and Technology of China, Hefei, Anhui 230026, China*

⁴*School of Physics and Astronomy, University of Leeds, Leeds LS2 9JT, UK*

⁵*Department of Physics, Southern University of Science and Technology, Shenzhen 518055, China*

⁶*INO-CNR BEC Center and Department of Physics,
University of Trento, Via Sommarive 14, I-38123 Trento, Italy*

(Dated: January 5, 2022)

The ongoing quest for understanding nonequilibrium dynamics of complex quantum systems underpins the foundation of statistical physics as well as the development of quantum technology. Quantum many-body scarring has recently opened a window into novel mechanisms for delaying the onset of thermalization, however its experimental realization remains limited to the \mathbb{Z}_2 state in a Rydberg atom system. Here we realize unconventional many-body scarring in a Bose–Hubbard quantum simulator with a previously unknown initial condition – the unit-filling state. Our measurements of entanglement entropy illustrate that scarring traps the many-body system in a low-entropy subspace. Further, we develop a quantum interference protocol to probe out-of-time correlations, and demonstrate the system’s return to the vicinity of the initial state by measuring single-site fidelity. Our work makes the resource of scarring accessible to a broad class of ultracold-atom experiments, and it allows to explore its relation to constrained dynamics in lattice gauge theories, Hilbert space fragmentation, and disorder-free localization.

Coherent manipulation of quantum many-body systems far from equilibrium is key to unlocking outstanding problems in quantum sciences including strongly-coupled quantum field theories, exotic phases of matter, and development of enhanced metrology and computation schemes. These efforts, however, are frequently plagued by the presence of interactions in such systems, which lead to fast thermalization and information scrambling – the behavior known as quantum ergodicity [1–3]. A twist came with recent advances in synthetic quantum matter, which enabled detailed experimental study of thermalization dynamics in isolated quantum many-body systems, leading to the observation of ergodicity-violating phenomena in integrable [4] and many-body localized systems [5, 6].

More recently, quantum many-body scarring has emerged as another remarkable ergodicity-breaking phenomenon, where preparing the system in special initial states effectively traps it in a “cold” subspace that does not mix with the thermalizing bulk of the spectrum [7, 8]. Such behavior hinders the scrambling of information encoded in the initial state and suppresses the spreading of quantum entanglement, allowing a many-body system to display persistent quantum revivals. Many-body scarring was first observed in the Rydberg atom experimental platform [9, 10] and subsequent observations of weak ergodicity breaking phenomena have attracted much attention [11–13]. On the other hand, theoretical works have unearthed universal scarring mechanisms [14–

17], pointing to the ubiquity of scarring phenomena in periodically-driven systems [18–20] and in the presence of disorder [21, 22]. However, due to its high sensitivity to initial states and the fragility of quantum many-body systems, the experimental implementation of quantum many-body scars beyond the \mathbb{Z}_2 state in Rydberg atom systems has remained elusive. It is thus vital to extend the realm of scarring to a greater variety of experimental platforms and more accessible initial conditions, which would empower fundamental understanding of nonergodic dynamics in various research areas ranging from lattice gauge theories to constrained glassy systems.

In this work, we observe many-body scarring in a large-scale Bose–Hubbard quantum simulator, where we employ a tilted optical lattice to emulate the PXP model, a canonical model of many-body scarring [23–26], see Fig. 1a. We demonstrate that a combination of detuning and periodic driving results in an unconventional many-body scarring regime in the unit-filling state, see Fig. 1b, hitherto believed to undergo fast thermalization [9]. Taking advantage of spin-dependent optical superlattices, we measure the system’s entanglement entropy by interfering identical copies in the double wells. We show the average entropy of single-site subsystems to be a good approximation of half-chain bipartite entropy, revealing a key property of scarring: the “trapping” of the quantum system in a low-entropy subspace, which prevents its relaxation into the exponentially large Hilbert space. Furthermore, we utilize the interference method to de-

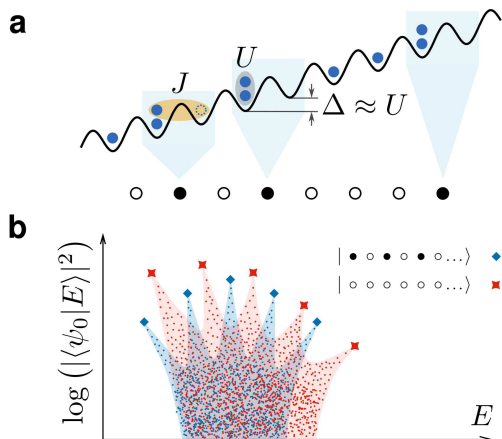


Figure 1. **Mapping the PXP model onto a Bose–Hubbard quantum simulator.** (a) At the $U \approx \Delta \gg J$ resonance, the only allowed hopping process is $11 \leftrightarrow 20$. The PXP excitations, \bullet , live on the bonds between the lattice sites. The doublon configuration 20 in the Bose–Hubbard model maps to an excitation in the PXP model, while all other configurations are mapped to an empty site, \circ . For example, the given state $|\dots \circ \bullet \bullet \circ \circ \bullet \bullet \dots\rangle$ maps to the Fock state $|\dots 120201120\dots\rangle$. (b) Scarred energy eigenstates $|E\rangle$ (blue diamonds) are distinguished by their high overlap on a special initial state $|\psi_0\rangle = |Z_2\rangle$. By detuning the Bose–Hubbard model, we bias the spectrum and realize a new scarring regime associated with the polarized state, $|0\rangle \equiv |\circ\circ\circ\dots\rangle$ (red crosses).

velop a protocol for measuring out-of-time correlations without brute-force tomography. We demonstrate this by measuring the single-site fidelity, which shows that scarring brings the system back to the vicinity of the initial state.

OBSERVATION OF Z_2 QUANTUM MANY-BODY SCARS

We first benchmark our quantum simulator on Z_2 quantum many-body scars [9]. We start by realizing the PXP model [27, 28], which describes a kinetically constrained chain of spin-1/2 degrees of freedom. Each spin can exist in two possible states, $|\circ\rangle$, $|\bullet\rangle$ corresponding to the ground state and excited state, respectively. An array of N such spins is governed by the Hamiltonian

$$\hat{H}_{\text{PXP}} = \Omega \sum_{j=1}^N \hat{P}_{j-1} \hat{X}_j \hat{P}_{j+1}, \quad (1)$$

where $\hat{X} = |\circ\rangle\langle\bullet| + |\bullet\rangle\langle\circ|$ is the Pauli x -matrix, describing local spin precession with frequency Ω . The projectors onto the ground state, $\hat{P} = |\circ\rangle\langle\circ|$, constrain the dynamics by allowing a spin to flip only if both of its neighbors are in the ground state.

In our quantum simulator, the PXP model is realized by tuning the on-site Hubbard interaction U to approx-

imately match the tilt potential Δ of the optical lattice [29, 30], a regime that has been studied extensively in the context of quantum Ising chains [31–33]. In the resonant regime $U \approx \Delta \gg J$, where J is the hopping amplitude, three-boson occupancy of any site is strongly suppressed, and doublons can only be created by moving a boson to the left, e.g., $\dots 11 \dots \rightarrow \dots 20 \dots$, or destroyed by moving a boson to the right, see Fig. 1a and Methods for details. The unit-filling state $|111\dots\rangle$ maps to the PXP polarized state $|0\rangle \equiv |\circ\circ\circ\dots\rangle$, while the state with doublons on every other site, $|2020\dots\rangle$, corresponds to $|Z_2\rangle \equiv |\bullet\circ\bullet\circ\dots\rangle$ state—the state containing the maximal number of excitations allowed by the constraint in the PXP model.

Remarkably, while the PXP model is quantum chaotic [23], preparing the system in a highly out-of-equilibrium $|Z_2\rangle$ initial state leads to persistent quantum revivals [34–36]. The presence of revivals due to a special initial state in an overall chaotic system was understood to be a many-body analog of the phenomena associated with a single particle inside a stadium billiard, where nonergodicity arises as a “scar” imprinted by a particle’s classical periodic orbit [16, 37, 38]. In many-body scarred systems, eigenstates were shown to form tower structures, illustrated in Fig. 1b. These towers are revealed by the anomalously high overlap of eigenstates with the initial state, such as $|Z_2\rangle$, and their equal energy spacing is responsible for quantum revivals.

We initialize the experiment by employing a superlattice in the y -direction to prepare a $\bar{n}=2$ Mott insulator in the left (odd) sites of the double wells with 99.2% fidelity, while removing all atoms on the right (even) sites via site-dependent addressing [39, 40]. This gives us the initial state $|\psi_0\rangle = |Z_2\rangle = |2020\dots\rangle$ (see Methods). The superlattice is formed by super-imposing the “short” lattice, with $a_s = 383.5$ nm spacing, and the “long” lattice, with $a_l = 767$ nm spacing. In the region of interest, we have prepared 50 copies of the initial state $|\psi_0\rangle$ isolated by the short lattice along the x -direction. Each copy extends over 50 short lattice sites along the y -direction. A pancake-shaped trap provides confinement in the z -direction. The short lattice in the y -direction makes an approximately 4° angle with gravity, which results in a static linear tilt per site of $\Delta_g = 816$ Hz. An external magnetic field gradient can be generated with coils, creating a controllable linear tilting potential together with gravity.

After initial-state preparation, the atoms are isolated in deep lattices with $60E_r$. $E_r = \hbar^2/8ma_s^2$ is the short-lattice recoil energy, where \hbar is the Planck constant and m is the ^{87}Rb atomic mass. We quench the system out of equilibrium by abruptly dropping the y -lattice depth to $11.6E_r$, which corresponds to switching J from 0 to $51(1)$ Hz. This is done while simultaneously adjusting the lattice depth in the x and z -directions accordingly, such that the interaction strength matches the linear tilt provided by gravity with $U = \Delta_g \approx 16J$. After evolution time t , we

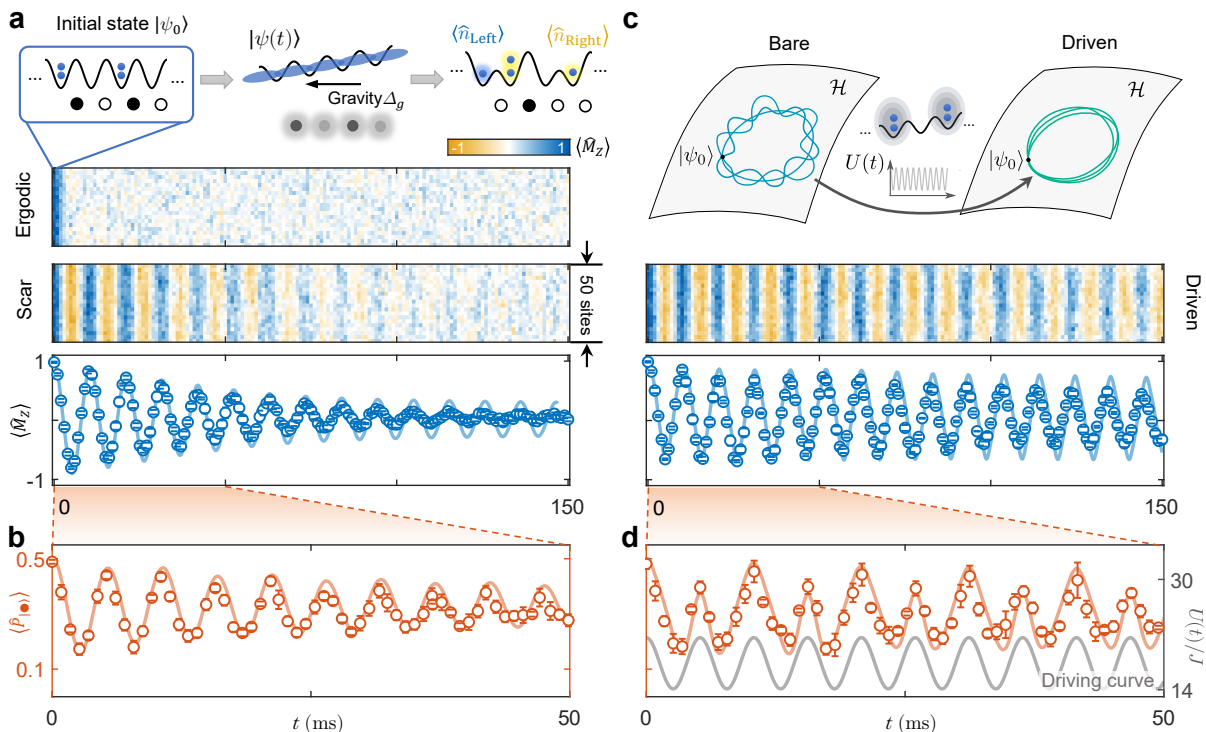


Figure 2. **Observation of \mathbb{Z}_2 quantum many-body scars in a Bose-Hubbard quantum simulator.** (a)-(b) Starting from the state $|\psi_0\rangle = |\dots 2020 \dots\rangle$, the analog of $|\mathbb{Z}_2\rangle$ state in the PXP model, we utilize gravity to provide linear tilt Δ_g . We characterize quench dynamics by measuring density imbalance and the number of doublons, corresponding to staggered magnetization $\langle \hat{M}_z \rangle$ and density of excitations $\langle \hat{P}_{|\bullet\rangle}$ in the PXP model. In the detuned regime $\Delta_g - U \approx -2J$, the dynamics is ergodic and the system has no memory of the initial state at late times. By contrast, tuning to $\Delta_g \approx U$, we observe persistent oscillations in both $\langle \hat{M}_z \rangle$ and $\langle \hat{P}_{|\bullet\rangle}$. This memory of the initial state is a signature of weak ergodicity breaking due to quantum many-body scars. (c)-(d) Periodic modulation of the interaction $U(t) = \Delta + U_0 + U_m \cos(\omega t)$ with $U_0 = 1.85J$, $U_m = 3.71J$, $\omega = 3.85J$ further suppresses the spreading of the wave function in the Hilbert space, leading to an enhancement of scarring. In both the static and driven case, experimental data for $\langle \hat{M}_z \rangle$ and $\langle \hat{P}_{|\bullet\rangle}$ are in excellent agreement with TEBD numerical simulations shown by blue and orange solid lines. Gray line shows the modulation $U(t)$.

freeze the dynamics and ramp up the double wells, where we read out the atomic density on the left and right sites of the y -superlattice successively with in-situ absorption imaging [40, 41]. This provides access to density imbalance, $\langle \hat{M}_z \rangle = (\langle \hat{n}_{\text{Left}} \rangle - \langle \hat{n}_{\text{Right}} \rangle) / (\langle \hat{n}_{\text{Left}} \rangle + \langle \hat{n}_{\text{Right}} \rangle)$, an observable corresponding to the staggered magnetization in the PXP model, see Fig. 2a. Another observable is the density of excitations in the PXP model, which is measured by projecting the number occupancy on each site into even (odd) parity, then reading out the average odd particle density $\langle \hat{P}_{|\bullet\rangle} \rangle_{(1)}$ [41]. Due to highly suppressed multi-boson occupancy, we have $\langle \hat{P}_{|\bullet\rangle} \rangle = \langle \hat{n}_{\text{doublon}} \rangle_{(1)} \approx (1 - \langle \hat{P}_{|\bullet\rangle} \rangle_{(1)})/2$.

Away from the resonance, the dynamics is ergodic and the staggered magnetization present in the initial $|\mathbb{Z}_2\rangle$ state quickly decays with time, see Fig. 2a. In contrast, in the vicinity of the resonance, $\Delta = U$, we observe distinct signatures of scarring: the system approximately undergoes persistent oscillations between the $|\mathbb{Z}_2\rangle \equiv |\bullet\bullet\bullet\dots\rangle$ configuration and its partner shifted by one site, $|\bar{\mathbb{Z}}_2\rangle \equiv |\circ\bullet\bullet\dots\rangle$, as can be seen in the staggered magnetization

profile and the density of excitations in Fig. 2b. The density of excitations does not distinguish between $|\mathbb{Z}_2\rangle$ and $|\bar{\mathbb{Z}}_2\rangle$ states, hence there is a trivial factor of 2 difference between the oscillation frequencies of $\langle \hat{P}_{|\bullet\rangle} \rangle$ and $\langle \hat{M}_z \rangle$.

The scarred oscillations in Fig. 2a are visibly damped with a decay rate γ , with $\gamma^{-1} = 49.6 \pm 0.8$ ms. Nevertheless, as shown in Ref. [10], by periodically driving the system it is possible to ‘refocus’ the spreading of the many-body wavefunction in the Hilbert space and thereby enhance the scarring effect, as we demonstrate in Fig. 2c-d. Crucially, this can be achieved without significantly altering the period of revivals. Our driving protocol is based on modulating the laser intensity of the z -lattice, which translates into periodic modulation of the interaction energy, $U(t) = \Delta + U_0 + U_m \cos(\omega t)$, while Δ is kept fixed. This results in a modulation of the density of doublons in the chain, acting as the analog of the chemical potential in the PXP model. For the driving parameters in Fig. 2c we find a strong enhancement of the amplitude of the oscillations in staggered magnetization with γ^{-1} increasing to 208 ± 10 ms, while the period remains

nearly the same as in the static case. Optimal driving parameters were determined numerically using a combination of simulated annealing and brute force search, see Supplementary Material (SM).

We note that the experimental measurement of $\langle \hat{M}_z \rangle$ damps slightly faster than the theory prediction, shown by a line in Fig. 2a, at late times ($t > 60$ ms). We attribute this to an inherent residual inhomogeneity across the lattice, which results in dephasing between different parts of the system, as well as possible decoherence induced by scattering of the lattice lasers. However, with driving we observe a significant increase in coherence time (Fig. 2c). To avoid the effect of these undesired dephasing or decoherence effects, in the following we limit our investigation up to 60 ms.

UNRAVELING THE DETAILS OF SCARRED DYNAMICS VIA QUANTUM INTERFERENCE

Fidelity and entanglement entropy are key observables for characterizing scarring behavior. These observables provide a window to the evolution of the system's wave function and the spreading of quantum entanglement. For a system trapped in a scarred subspace, thermalization is inhibited and the system exhibits suppressed entropy growth and periodic fidelity revivals. Measuring these observables usually requires brute-force state tomography, but for our 50-site Bose-Hubbard system with a Hilbert space dimension exceeding 10^{28} , this approach is generally impossible.

However, the superlattice in the x -direction allows us to probe these observables by interfering identical copies in the double wells, analogous to the 50 : 50 beam splitter (BS) interference employed in photonics experiments [42]; see Fig. 3a. This is done by freezing the dynamics along the chains in the y -direction after evolution time t , then we interfere copies of $|\psi(t)\rangle$ in the double wells formed by the x -superlattice (see Methods). After the interference, a parity projection helps read out the average odd particle density $\langle \hat{P}_{\tilde{n} \in \text{odd}}^{\text{BS}} \rangle_{(1)}$, which give us access to the second-order Rényi entropy [43]. Due to limitations in our imaging resolution, we were not able to access entropy in extensively large subsystems, however, we measured the entropy of single-site subsystems $S_{(1)} = -\ln(\text{Tr}_{(1)}[\hat{\rho}(t)^2]) = -\ln(1 - 2\langle \hat{P}_{\tilde{n} \in \text{odd}}^{\text{BS}} \rangle_{(1)})$, where $\hat{\rho}(t) = |\psi(t)\rangle \langle \psi(t)|$ is the density matrix. Due to the strong suppression of entanglement growth in a scarred system, we find $S_{(1)}$ serves as a good approximation for the half-chain bipartite entropy $S_{L/2}$, see Fig. 3b. Both single-site and half-chain entropy are seen to oscillate with the same frequency as $\langle \hat{P}_{\bullet} \rangle$, implying that the system returns to the neighborhood of product states $|\bar{Z}_2\rangle$ and $|\bar{Z}_2\rangle$. Our measurement of the Rényi entropy allows to identify a driving protocol that almost fully disconnects the scarred subspace from the thermalizing bulk of the spectrum, trapping the system in a vanishingly small

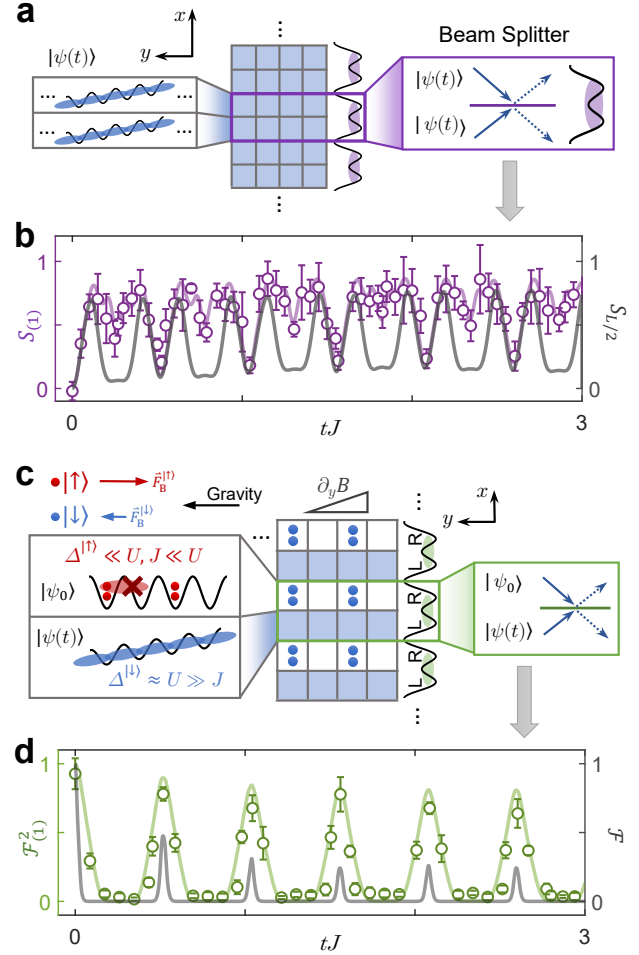


Figure 3. Probing many-body scarred dynamics via quantum interference. (a)-(b) After evolution time t , we freeze the dynamics in the y -direction, then by interfering two identical copies in the double wells along the x -direction, we obtain the second order Rényi entropy for a single site, $S_{(1)}$. The entropy is seen to have robust oscillations with the same frequency as in Fig. 2b, indicating a lack of thermalization at the single-site level. The single-site entropy is a good approximation to the half-chain entropy, $S_{L/2}$, evaluated numerically using TEBD (grey line). (c)-(d) We flip all right sites in the x -superlattice to the state $|\uparrow\rangle$, then by applying an external magnetic field gradient in the y -direction, we create state-dependent linear tilting with $\Delta_B^{|\uparrow\rangle} = -2\Delta_B^{|\downarrow\rangle}$. Fine tuning of the Hubbard parameters freezes the dynamics of $|\uparrow\rangle$ atoms, which are flipped back to $|\downarrow\rangle$ after evolution time t . We then interfere the left and right copies to read out single-site fidelity $\mathcal{F}_{(1)}$. The fidelity displays pronounced revivals, indicating periodic returns to the close vicinity of the initial state. Global fidelity, obtained numerically using TEBD, is shown by the grey line. Experimental data is for periodically driven systems with the same parameters as in Fig. 2d.

corner of an exponentially large Hilbert space.

Furthermore, we extend the interference protocol to probe unequal-time correlators. Before initiating the evolution, we first transfer atoms on the right sites of the

double wells in the x -superlattice to the internal state $|\uparrow\rangle = |F=2, m_F = -2\rangle$ while leaving the atoms on the left sites in the state $|\downarrow\rangle = |F=1, m_F = -1\rangle$, see Methods for details. By applying the magnetic field gradient, we generate a state-dependent linear tilt with $\Delta_B^{|\uparrow\rangle} = -2\Delta_B^{|\downarrow\rangle}$, see Fig. 3c. We fine-tune the magnetic field gradient, such that the $|\uparrow\rangle$ atoms are effectively “frozen” in the initial state $|\psi_0\rangle$, while evolving the chains along the left sites to $|\psi(t)\rangle$. We then interfere these copies of $|\psi_0\rangle$ and $|\psi(t)\rangle$ in the x -superlattice, and thus read out the single-site fidelity with $\mathcal{F}_{(1)} = \text{Tr}_{(1)}[\hat{\rho}_0\hat{\rho}(t)] = 1 - 2\langle\hat{P}_{n\in\text{odd}}^{\text{BS}}\rangle_{(1)}$. In Fig. 3d, we observe that $\mathcal{F}_{(1)}^2$ displays persistent revivals at the frequency of $\langle\hat{M}_z\rangle$, revealing the system’s periodic return to the vicinity of its initial state. The single-site fidelity $\mathcal{F}_{(1)}$ provides an upper bound for the global fidelity $\mathcal{F} = |\langle\psi_0|\psi(t)\rangle|^2$ for the quenches studied, and the two oscillate with the same frequency, as demonstrated numerically in Fig. 3d (see also SM).

EMERGENCE OF AN UNCONVENTIONAL SCARRING REGIME

Remarkably, we find that a combination of detuning and periodic drive can result in dynamical stabilization of a distinct scarring regime for initial states other than $|\mathbb{Z}_2\rangle$. We highlight this finding in experimental observations of scarring behavior in the polarized state $|0\rangle$, previously not associated with quantum many-body scars [9].

We start with the unit-filling state $|1111\dots\rangle$ in the lattice along the y -direction [39], which maps to the polarized state in the PXP model (see also Methods). In the absence of detuning or periodic drive, we observe fast relaxation: the density of excitations, single-site entropy, and fidelity all rapidly relax, with no visible oscillations beyond the timescale $\sim 1/J$, see Fig. 4a. Interestingly, when we bias the system by a static detuning, $U_0 = -2.38J$, we observe the emergence of oscillations in all three observables, accompanied by a slight decay, see Fig. 4b. Finally, if we also periodically modulate the interaction with amplitude $U_m = 1.54J$ and frequency $\omega = 4.9J \times 2\pi$, we find a dramatic enhancement of scarring, Fig. 4c. In particular, both entropy and fidelity now show pronounced oscillations, signaling robust scar-induced coherence at all experimentally-accessible times.

Our experimental observations are explained by theoretical analysis of the PXP model summarized in Figs. 4d, e, f. By computing the overlap of all energy eigenstates $|E\rangle$ of the PXP model in Eq. (1) with the polarized state $|\psi_0\rangle = |0\rangle$, we do not identify any hallmarks of scars, such as ergodicity-violating eigenstates with anomalously enhanced projection on $|0\rangle$, see Fig. 4d. On the other hand, when we add static detuning, which corresponds to the chemical potential in the PXP model, a band of scarred eigenstates with anomalously large overlap with $|0\rangle$ emerges; see Fig. 4e. Numerical simulations show that the PXP model remains chaotic for the

value of static detuning used in experiment (Fig. 4b), and this detuning is not large enough to trivially fragment the entire spectrum into disconnected sectors with the given numbers of excitations (see SM). The band of scarred eigenstates, illustrated by crosses in Fig. 4e, spans the entire energy spectrum, but their support on $|0\rangle$ is biased towards the ground state due to the breaking of particle-hole symmetry by detuning. We note that the scarred eigenstates in Fig. 4e are distinct from the known ones associated with the $|\mathbb{Z}_2\rangle$ state, but otherwise possess similar scarring properties such as anomalously low entanglement entropy (see SM). Finally, further enhancement of scarring under periodic modulation of the PXP chemical potential is explained by the spectrum of the corresponding Floquet operator, numerically evaluated in Fig. 4f. We observe that a single Floquet mode (denoted by a cross) develops a very large overlap with the $|0\rangle$ state. The existence of a single Floquet mode, whose mixing with other modes is strongly suppressed, gives rise to robust oscillations in the dynamics well beyond the experimentally accessible timescales.

DISCUSSION AND OUTLOOK

We performed a quantum simulation of the paradigmatic PXP model of many-body scarring using a tilted Bose–Hubbard optical lattice. We demonstrated the existence of persistent quantum revivals from the $|\mathbb{Z}_2\rangle$ initial state and their dynamical stabilization, opening up a new route for the investigation of scarring beyond Rydberg atom arrays. By harnessing the effect of detuning and periodic driving, we observed a distinct scarring regime associated with the polarized initial state. As the latter state is spatially homogeneous, its preparation does not require a superlattice, which makes further investigations of scarring phenomena accessible to a large class of ultracold atom experiments. The versatility of such platforms allows to directly probe the link between many-body scarring and other forms of ergodicity-breaking phenomena, such as Hilbert space fragmentation and disorder-free localization, as the latter can be conveniently studied in our setup by varying the tilt.

Our demonstration of scarring in the $|0\rangle$ state highlights the importance of energy density. While the $|\mathbb{Z}_2\rangle$ initial state has predominant support on the eigenstates in the middle of the spectrum, i.e., it constitutes an “infinite temperature” ensemble, the support of the $|0\rangle$ state is biased towards one end of the spectrum as result of particle-hole symmetry breaking via the detuning potential. This suggests that, depending on the effective temperature, one can realize scarring from a much larger class of initial states with a suitable choice of detuning and periodic driving protocols (see SM). Furthermore, one may expect realizations of qualitatively new scarring models by tuning to other resonance conditions and other types of lattices, including ladders and two-dimensional

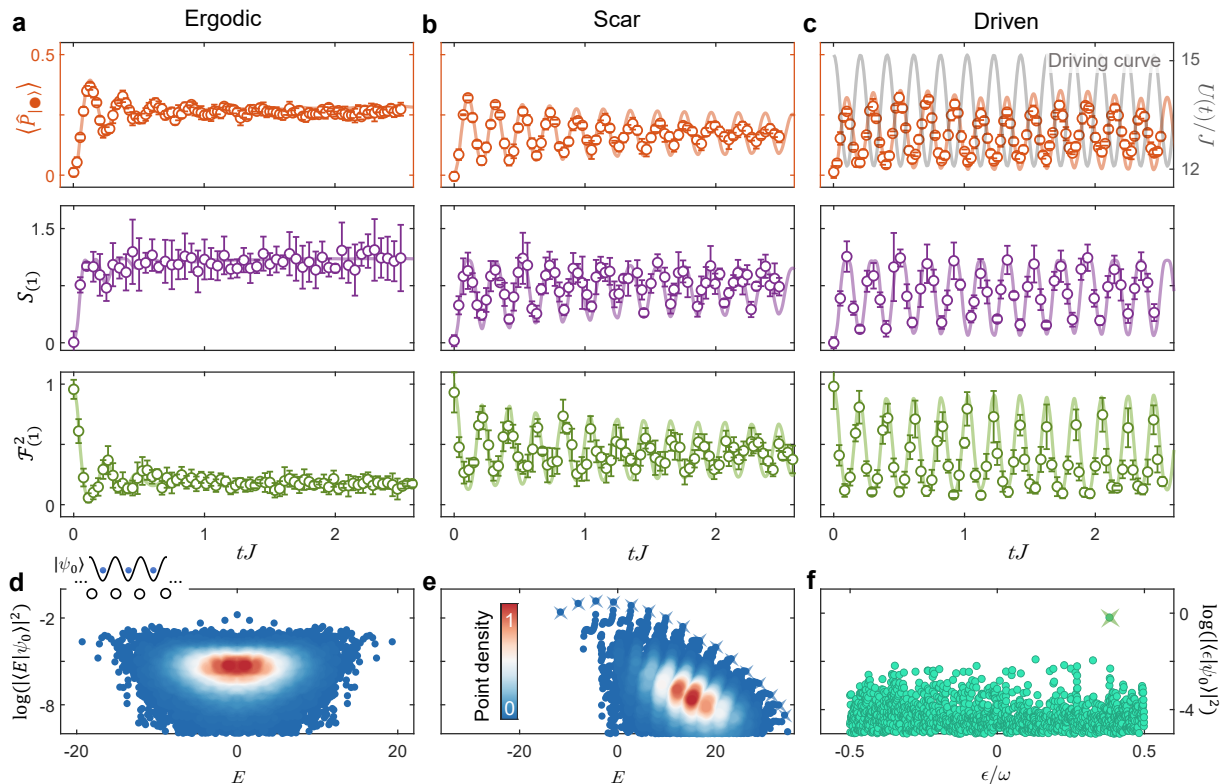


Figure 4. **Emergence of many-body scarring in the polarized state.** **a:** Fast thermalization from the unit-filling state in the Bose–Hubbard chain at $U=\Delta$ resonance. **b:** Emergence of scarred dynamics in the presence of static detuning. **c:** Dynamical stabilization of scarred dynamics in the presence of both detuning and periodic driving. Panels **a**, **b**, **c** are experimental measurements of the density of excitations, second Rényi entropy and fidelity for a single site. Static detuning is $U_0 = -2.38J$ and the modulation parameters are $U_m=1.54J$, $\omega=4.9J \times 2\pi$. Lines are the results of TEBD simulations. **d**, **e**, **f:** Exact diagonalization results for the PXP model. **d**, **e** show overlaps of all eigenstates with the polarized state in the PXP chain on a ring with $N=32$ sites. The value of static detuning in **e** matches that used in **b**. **f** shows the spectrum of the Floquet unitary for the PXP chain with $N=24$ sites and driving parameters corresponding to **c**.

arrays. While in 1D our Bose–Hubbard lattice with the staggered chemical potential can also be mapped to the quantum link model providing a different PXP realization [44], such a mapping does not directly extend to higher dimensions and potentially results in yet another class of scarred models.

Finally, our methods for probing unequal-time correlators allow for state-of-the-art monitoring of nonequilibrium dynamics and its applications in quantum technology. Notably, this protocol can be used to probe the global fidelity, as well as the out-of-time correlations between arbitrary quantum states, e.g., $|\langle \psi(t_1) | \psi(t_2) \rangle|^2$, with the help of single-atom resolution quantum gas microscopes [43, 45]. This would empower detailed experimental studies of exotic quantum phenomena such as dynamical quantum phase transitions [46]. The observation of long-lived quantum coherence due to scarring and its controllable enhancement via periodic modulation, lays the foundation for applications such as quantum memories and quantum sensing [47]. Moreover, the dynamical manipulation of a many-body system employed in

this work can be directly used to prepare states with extensive multipartite entanglement [48], thus lending itself to novel protocols for phase estimation and quantum metrology.

ACKNOWLEDGMENTS

We thank Philipp Hauke, Bhaskar Mukherjee, and Christopher Turner for useful discussions. The experiment is supported by the NNSFC 12125409, the Anhui Initiative in Quantum Information Technologies, and the Chinese Academy of Sciences. A.H., J.-Y.D., and Z.P. acknowledge support by EPSRC grant EP/R513258/1 and by the Leverhulme Trust Research Leadership Award RL-2019-015. A. H. acknowledges funding provided by the Institute of Physics Belgrade, through the grant by the Ministry of Education, Science, and Technological Development of the Republic of Serbia. Part of the numerical simulations were performed at the Scientific Computing Laboratory, National Center of Excellence for the Study of Complex Systems, Institute of Physics Bel-

grade. J.C.H. acknowledges support by Provincia Autonoma di Trento, the ERC Starting Grant StrEnQTh (project ID 804305), the Google Research Scholar Award ProGauge, and Q@TN – Quantum Science and Technology in Trento.

AUTHOR CONTRIBUTIONS

G.-X.S., H.S., Z.-Y.Z., Z.-S.Y., and J.-W.P. performed the experiment and analyzed the data. B.Y. participated in the discussions and offered suggestions to the experiment. A.H., J.Y.D., J.C.H., and Z.P. developed the theoretical proposal for the experiment and performed the theoretical analysis of the results. All authors contributed to the writing of the manuscript.

COMPETING INTERESTS

The authors declare no competing interests.

-
- [1] J. M. Deutsch, *Phys. Rev. A* **43**, 2046 (1991).
 [2] M. Srednicki, *Phys. Rev. E* **50**, 888 (1994).
 [3] M. Rigol, V. Dunjko, and M. Olshanii, *Nature* **452**, 854 (2008).
 [4] T. Kinoshita, T. Wenger, and D. S. Weiss, *Nature* **440**, 900 (2006).
 [5] R. Nandkishore and D. A. Huse, *Annual Review of Condensed Matter Physics* **6**, 15 (2015).
 [6] D. A. Abanin, E. Altman, I. Bloch, and M. Serbyn, *Rev. Mod. Phys.* **91**, 021001 (2019).
 [7] M. Serbyn, D. A. Abanin, and Z. Papić, *Nature Physics* **17**, 675 (2021).
 [8] S. Moudgalya, B. A. Bernevig, and N. Regnault, (2021), [arXiv:2109.00548 \[cond-mat.str-el\]](https://arxiv.org/abs/2109.00548).
 [9] H. Bernien, S. Schwartz, A. Keesling, H. Levine, A. Omran, H. Pichler, S. Choi, A. S. Zibrov, M. Endres, M. Greiner, V. Vuletić, and M. D. Lukin, *Nature* **551**, 579 (2017).
 [10] D. Bluvstein, A. Omran, H. Levine, A. Keesling, G. Semeghini, S. Ebadi, T. T. Wang, A. A. Michailidis, N. Maskara, W. W. Ho, S. Choi, M. Serbyn, M. Greiner, V. Vuletić, and M. D. Lukin, *Science* **371**, 1355 (2021).
 [11] W. Kao, K.-Y. Li, K.-Y. Lin, S. Gopalakrishnan, and B. L. Lev, *Science* **371**, 296 (2021).
 [12] S. Scherg, T. Kohlert, P. Sala, F. Pollmann, B. Hebbe Madhusudhana, I. Bloch, and M. Aidelsburger, *Nature Communications* **12**, 4490 (2021).
 [13] P. N. Jepsen, Y. K. Lee, H. Lin, I. Dimitrova, Y. Margalit, W. W. Ho, and W. Ketterle, “Catching Bethe phantoms and quantum many-body scars: Long-lived spin-helix states in Heisenberg magnets,” (2021), [arXiv:2110.12043 \[cond-mat.quant-gas\]](https://arxiv.org/abs/2110.12043).
 [14] S. Moudgalya, N. Regnault, and B. A. Bernevig, *Phys. Rev. B* **98**, 235156 (2018).
 [15] N. Shiraishi and T. Mori, *Phys. Rev. Lett.* **119**, 030601 (2017).
 [16] W. W. Ho, S. Choi, H. Pichler, and M. D. Lukin, *Phys. Rev. Lett.* **122**, 040603 (2019).
 [17] D. K. Mark, C.-J. Lin, and O. I. Motrunich, *Phys. Rev. B* **101**, 195131 (2020).
 [18] S. Sugiura, T. Kuwahara, and K. Saito, *Phys. Rev. Research* **3**, L012010 (2021).
 [19] K. Mizuta, K. Takasan, and N. Kawakami, *Phys. Rev. Research* **2**, 033284 (2020).
 [20] B. Mukherjee, S. Nandy, A. Sen, D. Sen, and K. Sengupta, *Phys. Rev. B* **101**, 245107 (2020).
 [21] I. Mondragon-Shem, M. G. Vavilov, and I. Martin, *PRX Quantum* **2**, 030349 (2021).
 [22] N. Shibata, N. Yoshioka, and H. Katsura, *Phys. Rev. Lett.* **124**, 180604 (2020).
 [23] C. J. Turner, A. A. Michailidis, D. A. Abanin, M. Serbyn, and Z. Papić, *Nature Physics* **14**, 745 (2018).
 [24] C.-J. Lin and O. I. Motrunich, *Phys. Rev. Lett.* **122**, 173401 (2019).
 [25] T. Iadecola, M. Schechter, and S. Xu, *Phys. Rev. B* **100**, 184312 (2019).
 [26] V. Khemani, C. R. Laumann, and A. Chandran, *Phys. Rev. B* **99**, 161101 (2019).
 [27] P. Fendley, K. Sengupta, and S. Sachdev, *Phys. Rev. B* **69**, 075106 (2004).
 [28] I. Lesanovsky and H. Katsura, *Phys. Rev. A* **86**, 041601 (2012).
 [29] S. Sachdev, K. Sengupta, and S. M. Girvin, *Phys. Rev. B* **66**, 075128 (2002).
 [30] K. Sengupta, “Phases and dynamics of ultracold bosons in a tilted optical lattice,” (2021), [arXiv:2109.02657 \[cond-mat.quant-gas\]](https://arxiv.org/abs/2109.02657).
 [31] F. Meinert, M. J. Mark, E. Kirilov, K. Lauber, P. Weinmann, A. J. Daley, and H.-C. Nägerl, *Phys. Rev. Lett.* **111**, 053003 (2013).
 [32] F. Meinert, M. J. Mark, E. Kirilov, K. Lauber, P. Weinmann, M. Gröbner, A. J. Daley, and H.-C. Nägerl, *Science* **344**, 1259 (2014).
 [33] J. Simon, W. S. Bakr, R. Ma, M. E. Tai, P. M. Preiss, and M. Greiner, *Nature* **472**, 307 (2011).
 [34] B. Sun and F. Robicheaux, *New Journal of Physics* **10**, 045032 (2008).
 [35] B. Olmos, M. Müller, and I. Lesanovsky, *New Journal of Physics* **12**, 013024 (2010).
 [36] C. J. Turner, A. A. Michailidis, D. A. Abanin, M. Serbyn, and Z. Papić, *Phys. Rev. B* **98**, 155134 (2018).
 [37] E. J. Heller, *Phys. Rev. Lett.* **53**, 1515 (1984).
 [38] C. J. Turner, J.-Y. Desaulles, K. Bull, and Z. Papić, *Phys. Rev. X* **11**, 021021 (2021).
 [39] B. Yang, H. Sun, C.-J. Huang, H.-Y. Wang, Y. Deng, H.-N. Dai, Z.-S. Yuan, and J.-W. Pan, *Science* **369**, 550 (2020).
 [40] B. Yang, H.-N. Dai, H. Sun, A. Reingruber, Z.-S. Yuan, and J.-W. Pan, *Phys. Rev. A* **96**, 011602 (2017).
 [41] B. Yang, H. Sun, R. Ott, H.-Y. Wang, T. V. Zache, J. C. Halimeh, Z.-S. Yuan, P. Hauke, and J.-W. Pan, *Nature* **587**, 392 (2020).
 [42] A. M. Kaufman, M. C. Tichy, F. Mintert, A. M. Rey, and C. A. Regal, *Advances in Atomic, Molecular and Optical Physics*, 1st ed., Vol. 67 (Elsevier Inc., 2018) pp. 377–427, [arXiv:1801.04670](https://arxiv.org/abs/1801.04670).
 [43] R. Islam, R. Ma, P. M. Preiss, M. Eric Tai, A. Lukin, M. Rispoli, and M. Greiner, *Nature* **528**, 77 (2015).
 [44] F. M. Surace, P. P. Mazza, G. Giudici, A. Lerose, A. Gambassi, and M. Dalmonte, *Phys. Rev. X* **10**, 021041 (2020).
 [45] W. S. Bakr, J. I. Gillen, A. Peng, S. Fölling, and

- M. Greiner, *Nature* **462**, 74 (2009).
- [46] P. Jurcevic, H. Shen, P. Hauke, C. Maier, T. Brydges, C. Hempel, B. P. Lanyon, M. Heyl, R. Blatt, and C. F. Roos, *Phys. Rev. Lett.* **119**, 080501 (2017).
- [47] S. Dooley, *PRX Quantum* **2**, 020330 (2021).
- [48] J.-Y. Desautels, F. Pietracaprina, Z. Papić, J. Goold, and S. Pappalardi, “Quantum many-body scars have extensive multipartite entanglement,” (2021), [arXiv:2109.09724 \[quant-ph\]](https://arxiv.org/abs/2109.09724).

METHODS

Mapping between PXP and Bose–Hubbard models

The Bose–Hubbard model in a tilted optical lattice is described by the Hamiltonian

$$\hat{H} = -J \sum_{i=1}^{L-1} \left(\hat{b}_i^\dagger \hat{b}_{i+1} + \hat{b}_{i+1}^\dagger \hat{b}_i \right) + \hat{U} + \hat{\Delta}, \quad (2)$$

where J is the hopping amplitude, \hat{b} , \hat{b}^\dagger are the standard Bose annihilation and creation operators, the interaction energy is $\hat{U} = (U/2) \sum_{i=1}^L \hat{n}_i (\hat{n}_i - 1)$, and tilt potential is $\hat{\Delta} = \Delta \sum_{i=1}^L i \hat{n}_i$. L denotes the number of sites in the chain and we assume open boundary conditions. Moreover, we fix the filling factor to $\nu=1$, i.e., the total number of bosons is also equal to L .

In order to realize the PXP model in the Bose–Hubbard quantum simulator, we tune the parameters to the resonant regime $U \approx \Delta \gg J$ [29, 30]. In this regime, three-boson occupancy of any site is strongly suppressed, and doublons can only be created by moving a particle to the left, e.g., $\dots 11 \dots \rightarrow \dots 20 \dots$, or destroyed by moving a particle to the right. The states of the PXP

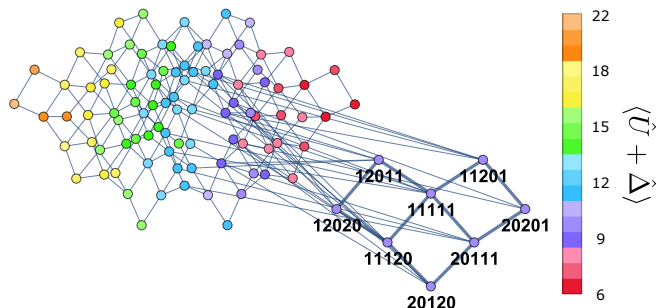


Figure M1. **Emergence of the PXP subspace in the Bose–Hubbard model at the resonance $U \approx \Delta \gg J$.** Dots represent Fock states of the tilted Bose–Hubbard model with 5 bosons on 5 sites (restricting to at most three bosons on any site). Lines denote the allowed hopping processes. The color scale shows the sum of interaction and tilt energies $\langle \hat{U} + \hat{\Delta} \rangle$ for each Fock state, and this value is conserved by resonant processes. The PXP dynamical subspace and its Fock states are explicitly labeled.

model are understood to live on the bonds of the Bose–Hubbard model. An excitation in the PXP model $\bullet_{j,j+1}$, living on the bond $(j, j+1)$, corresponds to the creation of a doublon $2_j 0_{j+1}$ on site j in the Bose–Hubbard chain. We identify the unit-filling state $|111\dots\rangle$ with the PXP polarized state, $|0\rangle \equiv |000\dots\rangle$. Any other configuration of the PXP model can be mapped to a Fock state in the Bose–Hubbard model by starting from the unit-filling, identifying the bonds that carry PXP excitations and replacing the corresponding sites in the Mott state with $11 \rightarrow 20$, see SM for further details. Applying this rule across the chain allows to map any basis state of the PXP model to a corresponding Fock state in the Bose–Hubbard model, e.g., the $|\mathbb{Z}_2\rangle$ state maps to the Fock state $|\dots 2020 \dots\rangle$. Fig. M1 illustrates the profound change in the connectivity of the Fock space near the resonance $U \approx \Delta \gg J$, with an emergent dynamical subspace isomorphic to the PXP model in the sector containing the $|\mathbb{Z}_2\rangle$ state.

State preparation and detection

Our experiment starts out with a two-dimensional Bose–Einstein condensate of ^{87}Rb atoms prepared in the hyperfine state $|\downarrow\rangle = 5S_{1/2} |F=1, m_F=-1\rangle$. By applying a microwave pulse, atoms can be adiabatically transferred to the state $|\uparrow\rangle = 5S_{1/2} |F=2, m_F=-2\rangle$, which is resonant with the imaging laser and thus can be detected. The atoms are initially confined to a single layer of a pancake-shaped trap with $3 \mu\text{m}$ period. In both x and y -directions, we have an optical superlattice that can be controlled separately. Each superlattice potential is generated by super-imposing two standing waves with laser frequency $\lambda_s=767 \text{ nm}$ and $\lambda_l=1534 \text{ nm}$, which can be described by

$$\begin{aligned} V(x) &= V_s^x \cos^2(kx) - V_l^x \cos^2(kx/2 + \theta_x) \\ V(y) &= V_s^y \cos^2(ky) - V_l^y \cos^2(ky/2 + \theta_y), \end{aligned} \quad (3)$$

where $V_s^{x(y)}$ is the depth of short (long) lattice in $x(y)$ -direction, $k=2\pi/\lambda_s$ is the short lattice wave number, and $\theta_{x(y)}$ the relative phase between the short and long lattices in $x(y)$ -direction.

We first perform a cooling technique by loading the atoms into a staggered superlattice in the y -direction at $\theta_y=\pi/4$, meanwhile ramping up only the short lattice in the x -direction. We tune the y -superlattice potential to create a Mott insulator with $\bar{n}=2$ filling in odd sites, while even sites form a $\bar{n}=1.5$ superfluid, serving as a reservoir for carrying away the thermal entropy [39].

Atoms in even sites are removed by performing site-selective addressing. This is done by first setting $\theta_y=0$ to form double wells, then tuning the polarization of the short lattice laser along the y -direction to create an energy splitting between even and odd sites for the $|\downarrow\rangle$ to $|\uparrow\rangle$ transition. We transfer the atoms in even sites to $|\uparrow\rangle$

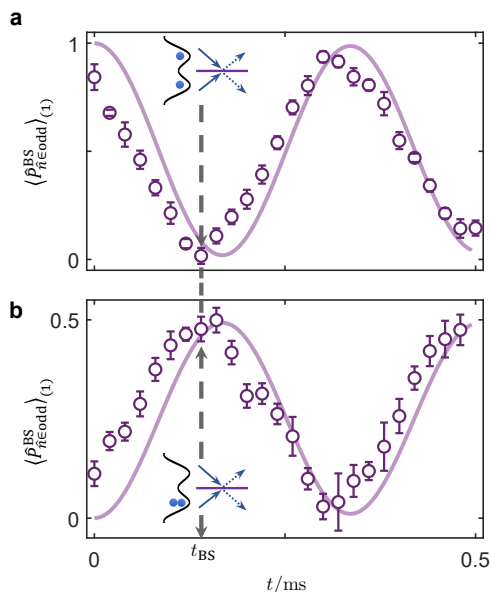


Figure M2. **Quantum interference.** (a) Interfering $|1,1\rangle$ product states in the double wells. (b) Interfering $|2,0\rangle$ product states in the double wells. Solid lines are TEBD simulations. Experimental data is shifted forward at earliest times due to the $50 \mu\text{s}$ ramping time of the lattice potential.

and remove them with the imaging laser [40]. This way we have prepared the initial $|\mathbb{Z}_2\rangle$ state $|2020\dots\rangle$. The same site-selective addressing procedure is also utilized to read out atomic density on even and odd sites separately in experiment. Inside each isolated double-well unit, we can perform state engineering that transfers the state $|2,0\rangle$ to $|1,1\rangle$ [39]. This results in the unit-filling state $|1111\dots\rangle$ which corresponds to the polarized state $|0\rangle$ in the PXP model.

Quantum interference in the double wells

The beam splitter (BS) interference is realized in the balanced double wells formed by the superlattices in the x -direction, expressed in Eq. (3) by setting $\theta_x=0$. In the non-interacting limit, indistinguishable bosonic particles coming into the the interference at $t=0$ interfere according to the bosonic bunching. Therefore, equal number of atoms coming into the two ports at $t=0$ results in $\langle \hat{P}_{\hat{n} \in \text{odd}}^{\text{BS}} \rangle = 0$ at t_{BS} , while different number of atoms interfering results in $\langle \hat{P}_{\hat{n} \in \text{odd}}^{\text{BS}} \rangle = 0.5$. Each copy of atoms coming into the interference are prepared individually, hence no global phase between them, resulting in the equivalence between the two output ports [43].

To implement the quantum interference protocol, we quench the x -lattice potentials to $V_s^x=6E_r$ and $V_l^x=5E_r$, resulting in the intra-double-well tunneling at $J \approx 740$ Hz and inter-double-well tunneling $J' \approx 35$ Hz. Simultaneously, we lower the lattice depth in the x -direction to $25E_r$ and trapping frequency in the z -direction to 1.4

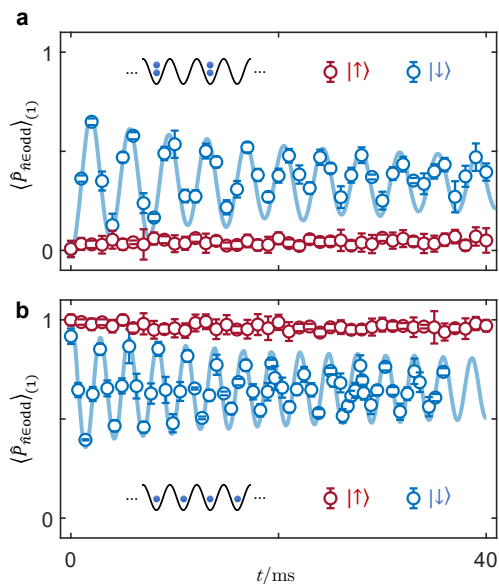


Figure M3. **Internal-state-dependent evolution.** (a) Starting from the initial $|\mathbb{Z}_2\rangle$ state, chains with $|\uparrow\rangle$ atoms remain largely at $\langle \hat{P}_{\hat{n} \in \text{odd}} \rangle_{(1)} \approx 0$ indicating they remain “frozen” in the initial state, while $|\downarrow\rangle$ atoms evolve with the scarred dynamics. (b) Starting from the initial polarized state $|0\rangle$, chains with $|\uparrow\rangle$ atoms remain largely at $\langle \hat{P}_{\hat{n} \in \text{odd}} \rangle_{(1)} \approx 1$, while the $|\downarrow\rangle$ atoms exhibit scarred dynamics in the presence of static detuning.

kHz, achieving an interaction of $U \approx 360$ Hz. Two examples are shown here in Fig. M2, where we interfere product states $|1,1\rangle$ (Fig. M2a) or $|2,0\rangle$ (Fig. M2b) in the double wells and read out the average odd particle density. At $t_{\text{BS}}=0.14$ ms we identify the beam splitter operation, where $|1,1\rangle$ gives $\langle \hat{P}_{\hat{n} \in \text{odd}}^{\text{BS}} \rangle_{(1)} = 0.01(3)$, while $|2,0\rangle$ gives $\langle \hat{P}_{\hat{n} \in \text{odd}}^{\text{BS}} \rangle_{(1)} = 0.48(3)$. We simulate the interference dynamics with a 20-site chain consisting of 10 double-well units. We find good agreement at later times, while the earlier times are affected by the finite time in the lowering and rising of lattice potentials, which takes $50 \mu\text{s}$. The finite interaction strength and inter-double-well tunneling results in about 1% error in the beam splitter operation in the simulation, but this is beyond the precision of our absorption imaging.

Internal-state-dependent evolution

We use site-selective addressing in the x -superlattice to transfer all right sites to the internal hyperfine state $|\uparrow\rangle$ with a microwave pulse, while leaving all left sites in $|\downarrow\rangle$ [40]. By applying an external magnetic-field gradient in the y -direction $\partial_y B$, the magnetic energy shift between nearest-neighbor short lattice sites of different hyperfine states can be described by the anomalous Zeeman effect

$$\Delta_{\text{B}}^{|F, m_F\rangle} = \mu_{\text{B}} \times g_{\text{F}} \times m_{\text{F}} \times \partial_y B \times a_{\text{s}}, \quad (4)$$

where μ_B is the Bohr magneton, the Landé factor g_F is 1/2 for $|\uparrow\rangle$, and -1/2 for $|\downarrow\rangle$. Therefore, we create a state-dependent linear potential with $\Delta_B^{|\uparrow\rangle} = -2\Delta_B^{|\downarrow\rangle}$. We fine-tune the gradient strength for different initial conditions such that the total linear potential $\Delta^{|\uparrow\rangle} = \Delta_g^{|\uparrow\rangle} - |\Delta_B^{|\uparrow\rangle}| \ll U$ would avoid resonant processes while suppressing the direct tunneling. Hence, atoms in the $|\uparrow\rangle$ state are “frozen” in the initial states during the entire evolution. To minimize the “leak” from the initial states, the Hubbard parameters are optimized experimentally by measuring the odd particle density $\langle \hat{P}_{\hat{n} \in \text{odd}} \rangle_{(1)}$. For the initial $|\mathbb{Z}_2\rangle$ state, $\langle \hat{P}_{\hat{n} \in \text{odd}} \rangle_{(1)}$ should remain close to 0, while for the polarized state $|0\rangle$, $\langle \hat{P}_{\hat{n} \in \text{odd}} \rangle_{(1)}$ should remain close to 1. We find the optimum magnetic field gradient for $|\mathbb{Z}_2\rangle$ state to be $\partial_y B \approx 11.5$ G/cm, corresponding to $\Delta^{|\uparrow\rangle} \approx 200$ Hz, meanwhile, the $|\downarrow\rangle$ atoms feel an increased linear potential with $\Delta^{|\downarrow\rangle} = \Delta_g^{|\downarrow\rangle} + |\Delta_B^{|\downarrow\rangle}| \approx 1120$ Hz, where we adjust the interaction U and tunneling J such that $\Delta^{|\downarrow\rangle} \approx U \approx 16J$, which give rise to the scarred dynamics, see Fig. M3a. For the polarized state, however, $\partial_y B \approx 14.3$ G/cm and $\Delta^{|\uparrow\rangle} \approx 50$ Hz results in better freezing of the $|\uparrow\rangle$ atoms, therefore we set $U \approx \Delta^{|\downarrow\rangle} \approx 1200$ Hz, see Fig. M3b. In both cases we find around 3% “leaking” from the initial states within the investigation time we measure single-site fidelity. This leaking contributes to the small deviation in single-site fidelity we find between experiments and TEBD simulations in Fig. 3 and Fig. 4.

After evolution time t , chains with $|\downarrow\rangle$ atoms have evolved to $|\psi(t)\rangle$, while chains with $|\uparrow\rangle$ atoms have largely remained in $|\psi_0\rangle$. We ramp up the short lattice in the y -direction to freeze the dynamics of $|\downarrow\rangle$ atoms along the chains, and flip all $|\uparrow\rangle$ atoms back to $|\downarrow\rangle$. Then interfere copies of $|\psi_0\rangle$ and $|\psi(t)\rangle$ in the double wells formed by the x -superlattice. After the parity projection, we read out single-site fidelity with $\mathcal{F}_{(1)} = \text{Tr}_{(1)}[\hat{\rho}_0 \hat{\rho}(t)] = 1 - 2\langle \hat{P}_{\hat{n} \in \text{odd}}^{\text{BS}} \rangle_{(1)}$.

— Supplementary Material —
**Observation of unconventional many-body
scarring in a quantum simulator**

CONTENTS

Mapping the tilted 1D Bose-Hubbard onto the PXP model	1
$\Delta \approx U$ resonance: first order terms	1
Higher order terms in the mapping	2
Numerical methods	3
Numerical demonstrations of the mapping between PXP and tilted Bose-Hubbard model	3
Global vs. single-site fidelity	4
Alternative mapping between PXP and tilted 1D Bose-Hubbard with staggered detuning	6
Effect of periodic driving on \mathbb{Z}_2 scars	7
Driven PXP model	7
Driving the tilted 1D Bose-Hubbard model	9
Quantum many-body scars in the polarized state	10
Pure PXP model	10
Static detuning in the PXP model	11
Periodic driving in the PXP model	12
Detuning and periodic driving in the tilted Bose-Hubbard model	13
Other quantum many-body scarred states	13
Effect of detuning on the spectral statistics of the PXP model	14
System-size scaling of the revival fidelity	15
References	17

**MAPPING THE TILTED 1D BOSE-HUBBARD
ONTO THE PXP MODEL**

In the main text and throughout this Supplementary Material, we study the 1D Bose-Hubbard model with linear tilt potential and open boundary conditions, described by the Hamiltonian

$$\hat{H} = -J \sum_{i=1}^{L-1} \left(\hat{b}_i^\dagger \hat{b}_{i+1} + \hat{b}_{i+1}^\dagger \hat{b}_i \right) + \frac{U}{2} \sum_{i=1}^L \hat{n}_i (\hat{n}_i - 1) + \Delta \sum_{i=1}^L i \hat{n}_i, \quad (\text{S1})$$

$\underbrace{\hspace{10em}}_{\hat{H}_U} \qquad \underbrace{\hspace{10em}}_{\hat{H}_\Delta}$

where J is the hopping amplitude, U is the interaction strength, Δ is the tilt and L the number of sites. Unless specified otherwise, we fix the filling factor to $\nu = 1$, i.e., the number of bosons is equal to the number of sites in the chain.

$\Delta \approx U$ resonance: first order terms

In the $U, \Delta \gg J$ limit, the energy spectrum of the Hamiltonian in Eq. (S1) splits into bands with approximately constant expectation value of the diagonal terms, $\langle \hat{H}_U + \hat{H}_\Delta \rangle \approx \text{const}$, and the Hilbert space becomes fragmented. At the $U \approx \Delta \gg J$ resonance, the only process which conserves $\langle \hat{H}_U + \hat{H}_\Delta \rangle$ is $11 \leftrightarrow 20$, i.e. doublons can only be created by moving a particle to the left and destroyed by moving a particle to the right. In the connected component of the Fock state $111 \dots 111$, the system in the resonant regime can therefore be described by an effective Hamiltonian

$$\hat{H}_{\text{eff}} = -J \sum_{i=1}^{L-1} \left(\hat{b}_i^\dagger \hat{b}_{i+1} \hat{n}_i (2 - \hat{n}_i) \hat{n}_{i+1} (2 - \hat{n}_{i+1}) + \text{h.c.} \right). \quad (\text{S2})$$

The Hamiltonian (S2) is equivalent to the PXP Hamiltonian [S1, S2], as will be shown below (see also Ref. [S3] for the original derivation of the mapping and a recent review [S4]).

The connected component of the Hilbert space contains only certain types of two-site configurations (20, 11, 12, 02, 01), while all other two-site configurations are forbidden (22, 21, 10, 00). If we consider the configuration 20 to be an excitation, all allowed configurations can be mapped to those of the PXP model as follows:

$$\begin{aligned} \dots 20 \dots &\leftrightarrow \circ \bullet \circ \\ \dots 11 \dots &\leftrightarrow \circ \circ \circ \\ \dots 12 \dots &\leftrightarrow \circ \circ \bullet \\ \dots 02 \dots &\leftrightarrow \bullet \circ \bullet \\ \dots 01 \dots &\leftrightarrow \bullet \circ \circ \end{aligned} \quad (\text{S3})$$

Note that excitations live on the bonds between sites and this mapping also includes links to the two surrounding sites. For example, the configuration $\dots 2020 \dots$ maps to $\circ \bullet \circ \bullet \circ$ and not to $\circ \bullet \circ \bullet \circ \bullet$. On the other hand, the configuration 2020 with open boundaries on both sides maps to $\bullet \circ \bullet$, as there are no bonds across the boundaries.

The effective Hamiltonian (S2) can be rewritten as:

$$\hat{H}_{\text{eff}} = -J \sum_{i=1}^{L-1} \left(\underbrace{\hat{b}_i^\dagger \hat{b}_{i+1} \delta_{\hat{n}_i, 1} \delta_{\hat{n}_{i+1}, 1}}_{\sqrt{2} \hat{P}_{j-1} \hat{\sigma}_j^+ \hat{P}_{j+1}} + \underbrace{\hat{b}_{i+1}^\dagger \hat{b}_i \delta_{\hat{n}_i, 2} \delta_{\hat{n}_{i+1}, 0}}_{\sqrt{2} \hat{P}_{j-1} \hat{\sigma}_j^- \hat{P}_{j+1}} \right). \quad (\text{S4})$$

In this equation, the index i labels the sites, while j labels the bonds between sites. The Kronecker delta functions have been expressed in terms of projectors, $\hat{P}_j = |\circ_j\rangle\langle\circ_j|$, and the bosonic hopping terms correspond to the spin raising and lowering operators, $\hat{\sigma}_j^\pm$, on the bond j . We can use delta functions because there are no configurations with more than 2 particles per site in this connected component and the only possible values of $\hat{n}_i(2 - \hat{n}_i)$ are 0 and 1. Moving a particle to a neighboring site on the left corresponds to creating an excitation, moving to the right to annihilating, while the delta functions act as constraints.

Finally, the effective Hamiltonian is therefore equivalent to the PXP Hamiltonian

$$\begin{aligned} \hat{H}_{\text{PXP}} &= \Omega \sum_{j=1}^N \left(\hat{P}_{j-1} \hat{\sigma}_j^+ \hat{P}_{j+1} + \hat{P}_{j-1} \hat{\sigma}_j^- \hat{P}_{j+1} \right) \\ &= \Omega \sum_{j=1}^N \hat{P}_{j-1} \hat{X}_j \hat{P}_{j+1}, \end{aligned} \quad (\text{S5})$$

when $\Omega = \sqrt{2}J$ and $N = L - 1$, where $\hat{X}_j \equiv |\circ_j\rangle\langle\bullet_j| + |\bullet_j\rangle\langle\circ_j|$ is the usual Pauli x matrix. In case of open boundary conditions (OBC) the two boundary terms become $\hat{X}_1 \hat{P}_2$ and $\hat{P}_{N-1} \hat{X}_N$. Note that the effective bosonic model for system size L is equivalent to the PXP model for size $N = L - 1$ since the number of bonds is the number of sites minus one.

In the PXP model, the initial states which lead to pronounced quantum revivals are the two states with the maximal number of excitations – the Néel states, $\bullet\bullet\bullet\circ\dots\bullet\circ$ and $\circ\bullet\bullet\circ\dots\bullet\bullet$ [S5, S6]. The equivalent states in the tilted Bose-Hubbard model are 2020...201 and 12020...20 for odd system sizes and 2020...20 and 120...201 for even sizes. In our experimental setup, it is not possible to exactly prepare the 2020...201 state due to the inability to independently control single sites. Instead, our experiment realizes the 2020...20 state, which corresponds to the Néel state $\bullet\bullet\bullet\circ\dots\bullet\bullet$ in the PXP model with an odd number of sites and open boundary conditions.

Higher order terms in the mapping

The effective Hamiltonian of Eq. (S2) results from the first-order Schrieffer-Wolff transformation [S7] where $\hat{H}_0 = \hat{H}_U + \hat{H}_\Delta$. In this section we look at the relevant terms that arise in the effective Hamiltonian at second order. To simplify the notation we write these terms as sums of range-3 operators, where $|111\rangle\langle 120|_j$ denotes the operator changing sites $j-1$, j and $j+1$ from 120 to 111 while leaving all other sites unaffected.

First, we can identify the matrix elements that take the system out of the PXP sector. This happens by the

appearance of sites with 3 bosons via the operator

$$\begin{aligned} \hat{H}_{\text{out}} &= \frac{\sqrt{3}J^2}{U} \sum_{j=2}^{L-1} \left(|300\rangle\langle 201|_j + |201\rangle\langle 300|_j \right. \\ &\quad \left. + 2|300\rangle\langle 120|_j + 2|120\rangle\langle 300|_j \right). \end{aligned} \quad (\text{S6})$$

There are also off-diagonal matrix elements connecting states within the PXP sector, given by

$$\hat{H}_{\text{OD}} = \frac{2J^2}{U} \sum_{j=2}^{L-1} \left(|120\rangle\langle 201|_j + |201\rangle\langle 120|_j \right). \quad (\text{S7})$$

There are also additional off-diagonal matrix elements connecting states outside of the PXP sector, but as they do not directly influence the dynamics out of it we do not describe them here.

Finally, the diagonal operator in this sector is given by

$$\begin{aligned} \hat{H}_{\text{Diag}} &= \frac{J^2}{U} \sum_{j=2}^{L-1} \left(4|120\rangle\langle 120|_j - |111\rangle\langle 111|_j \right. \\ &\quad \left. + |020\rangle\langle 020|_j - |112\rangle\langle 112|_j \right) \\ &\quad + \frac{J^2}{U} \left(|01\rangle\langle 01|_{L-1} - |11\rangle\langle 11|_1 - |12\rangle\langle 12|_1 \right), \end{aligned} \quad (\text{S8})$$

where the two-site operator $|11\rangle\langle 12|_j$ acts on sites j and $j+1$. As bulk terms get added, the overall diagonal factors are extensive in the system size in the Fock basis. The state with the lowest on-site potential is $|111\dots 11\rangle$ with a value of $-\frac{(L-1)J^2}{U}$. The maximum is $\approx \frac{4J^2L}{3U}$ for the state $|120120\dots 120\rangle$, which corresponds to the \mathbb{Z}_3 state in the PXP terminology.

In order to see how these second-order terms change the effective model we can rewrite Eqs. (S7)-(S8) for the PXP model with $N = L - 1$ sites. To do this we introduce the single-site projector on the excited state $\hat{Q}_j = |\bullet\rangle\langle\bullet| = \mathbf{1} - \hat{P}_j$. We then obtain

$$\begin{aligned} \hat{H}_{\text{OD}}^{\text{PXP}} &= \frac{2J^2}{U} \sum_{j=1}^{N-2} \left(\hat{P}_{j-1} \hat{\sigma}_j^+ \hat{\sigma}_{j+1}^- \hat{P}_{j+2} + \hat{P}_{j-1} \hat{\sigma}_j^- \hat{\sigma}_{j+1}^+ \hat{P}_{j+2} \right) \\ &\quad + \frac{2J^2}{U} \left(\hat{\sigma}_1^+ \hat{\sigma}_2^- \hat{P}_3 + \hat{\sigma}_1^- \hat{\sigma}_2^+ \hat{P}_3 \right) \\ &\quad + \frac{2J^2}{U} \left(\hat{P}_{N-3} \hat{\sigma}_{N-1}^+ \hat{\sigma}_N^- + \hat{P}_{N-2} \hat{\sigma}_{N-1}^- \hat{\sigma}_N^+ \right) \end{aligned} \quad (\text{S9})$$

and

$$\begin{aligned}
\hat{H}_{\text{Diag}}^{\text{PXP}} = & \frac{J^2}{U} \sum_{j=1}^{N-2} (4\hat{P}_{j-1}\hat{P}_j\hat{Q}_{j+1}\hat{P}_{j+2} - \hat{P}_{j-1}\hat{P}_j\hat{P}_{j+1}\hat{P}_{j+2} \\
& + \hat{Q}_{j-1}\hat{P}_j\hat{Q}_{j+1}\hat{P}_{j+2} - \hat{P}_{j-1}\hat{P}_j\hat{P}_{j+1}\hat{Q}_{j+2}) \\
& + \frac{J^2}{U} (4\hat{P}_0\hat{Q}_1\hat{P}_2 - \hat{P}_0\hat{P}_1\hat{P}_2 - \hat{P}_0\hat{P}_1\hat{Q}_2 \\
& + 4\hat{P}_{N-2}\hat{P}_{N-1}\hat{Q}_N - \hat{P}_{N-2}\hat{P}_{N-1}\hat{P}_N \\
& + \hat{Q}_{N-2}\hat{P}_{N-1}\hat{Q}_N) \\
& + \frac{J^2}{U} (\hat{Q}_{N-1}\hat{P}_N - \hat{P}_0\hat{P}_1 - \hat{P}_0\hat{Q}_1), \tag{S10}
\end{aligned}$$

respectively. We notice that the off-diagonal correction has the form of a constrained XY term.

NUMERICAL METHODS

In the main text and this Supplementary Material, we use two types of numerical methods for modeling the experiment. For small Bose-Hubbard chains with $L \lesssim 12$ sites, we use exact diagonalization techniques to obtain the full energy spectrum of the Hamiltonian and directly access the system's eigenstate properties. Unless specified otherwise, we restrict the occupancy of any site to be at maximum 3 bosons, as our results are found to be insensitive to allowing more than 3 bosons on any site.

To access dynamics in much larger systems, $L \lesssim 50$ sites, we use TEBD variational method [S8] implemented in TenPy package [S9]. We employ the second order Trotter decomposition with time step $2.5 \times 10^{-5}/J$ and maximum bond dimension $\chi_{\text{max}} = 3000$. Such a small time step was necessary because some of the quantities we are interested in, e.g., the fidelity density, are sensitive to otherwise negligible fluctuations in the revival peak heights that appear for longer time steps.

For numerical simulations via either one of these methods, it is convenient to work in natural units $\hbar=1$. We adopt this convention for presenting all numerical results in this Supplementary Material.

Numerical demonstrations of the mapping between PXP and tilted Bose-Hubbard model

In this Section, we numerically corroborate the mapping between PXP and Bose-Hubbard models introduced in Sec. . Specifically, we use exact diagonalization to demonstrate the consistency between dynamics and eigenstate properties in the PXP model and the Bose-Hubbard model tuned to the resonance $U=\Delta$.

In analogy with the PXP model, the system initialized in the state $2020\dots 201$ is expected to oscillate between this state and the state $12020\dots 20$. This is not only the

case for the effective model (S4) which is exactly equivalent to PXP, but also for the full tilted Bose-Hubbard model (S1) at the $U = \Delta$ resonance, as can be observed in Fig. S1.

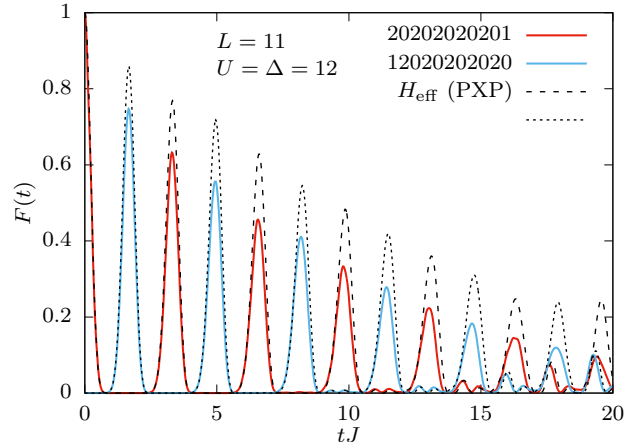


Figure S1. Evolution of quantum fidelity $F(t) = |\langle \psi_0 | e^{-iHt} | \psi_0 \rangle|^2$ starting from the state $|\psi_0\rangle = |2020\dots 201\rangle$ (red) and the amplitude of state transfer, $\mathcal{O}(t) = |\langle \psi | e^{-iHt} | \psi_0 \rangle|^2$, with the state $|\psi\rangle = |12020\dots 2020\rangle$ (blue). The evolution is governed by the tilted Bose-Hubbard Hamiltonian in Eq. (S1) with $J=1$, $U=\Delta=12$ and maximally 3 particles per site. The dashed and dotted black lines correspond to the effective model in Eq. (S4). System size $L=11$, filling factor $\nu=1$.

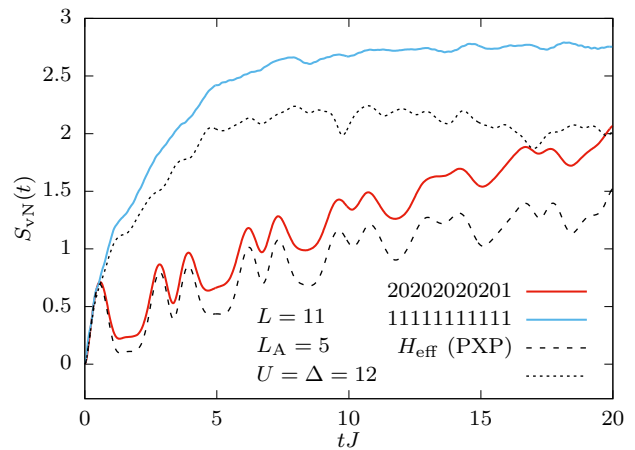


Figure S2. Evolution of the bipartite entanglement entropy for the initial states $|2020\dots 201\rangle$ (red) and $|111\dots 111\rangle$ (blue). The evolution is governed by the tilted Bose-Hubbard Hamiltonian from Eq. (S1) with $J = 1$, $U = \Delta = 12$ and maximally 3 particles per site. The dashed and dotted black lines correspond to the effective model from Eq. (S4). System size $L = 11$, subsystem $L_A = 5$, filling factor $\nu = 1$.

In Fig. S2 we show the evolution of the bipartite von Neumann entanglement entropy, $S_{\text{vN}}(t) = -\text{Tr}_A(\hat{\rho}_A \ln \hat{\rho}_A)$, where $\hat{\rho}_A$ is the reduced density matrix for subsystem A of length L_A . The system is initially

prepared in the state 2020...201 or the completely homogeneous state 111...111. As in the PXP model, the entanglement entropy for the 2020...201 state exhibits slow and approximately linear growth in time. In contrast, the entanglement entropy for the state 111...111 rapidly saturates, implying that the system quickly thermalizes.

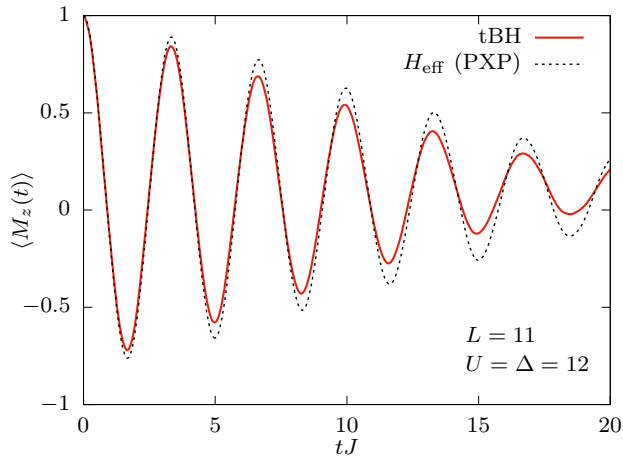


Figure S3. Evolution of staggered magnetization $\langle \hat{M}_z \rangle = (\langle \hat{n}_{\text{odd}} \rangle - \langle \hat{n}_{\text{even}} \rangle) / (\langle \hat{n}_{\text{odd}} \rangle + \langle \hat{n}_{\text{even}} \rangle)$, where \hat{n}_{odd} and \hat{n}_{even} are the numbers of particles on odd and even sites. The evolution is governed by the tilted Bose-Hubbard Hamiltonian from Eq. (S1) with $J = 1$ and $U = \Delta = 12$ (solid red line) and the effective model from Eq. (S4) which is equivalent to the PXP model (dashed black line). System size $L = 11$, filling factor $\nu = 1$, initial state $|2020\dots201\rangle$.

The evolution of density imbalance between the even and odd sites $\langle \hat{M}_z \rangle = (\langle \hat{n}_{\text{odd}} \rangle - \langle \hat{n}_{\text{even}} \rangle) / (\langle \hat{n}_{\text{odd}} \rangle + \langle \hat{n}_{\text{even}} \rangle)$, which corresponds to staggered magnetization in the PXP model, is shown in Fig. S3. This is one of the quantities that was experimentally measured in the main text. Here we again compare the evolution with the full tilted Bose-Hubbard Hamiltonian (S1) and the effective Hamiltonian (S4), the latter being equivalent to the PXP model, and we find excellent agreement between the two.

The overlap of eigenstates in the full model in Eq. (S1) for a chain of $L = 9$ sites with the initial 202020201 state is given in Fig. S4. For parameter values $U = \Delta = 12$, and $J = 1$, the energy spectrum is split into multiple bands with approximately constant expectation value of the sum of interaction and tilt terms $\langle \hat{H}_U + \hat{H}_\Delta \rangle$, as indicated by different colors. The inset shows the top part of the highest-overlap band (around $E = \langle 202020201 | \hat{H} | 202020201 \rangle = 432$). This band is described by the effective Hamiltonian (S2), which preserves the expectation value $\langle \hat{H}_U + \hat{H}_\Delta \rangle$ and is equivalent to the PXP Hamiltonian. A band of $L = 9$ scarred eigenstates is visible in the inset, as expected from the analogy with the PXP model. These scarred eigenstates are responsible for the revival dynamics in Fig. S1. As the two Néel states have the maximal number of dou-

blons at filling factor $\nu = 1$, this type of dynamics also leads to oscillations in doublon number, which can be experimentally measured.

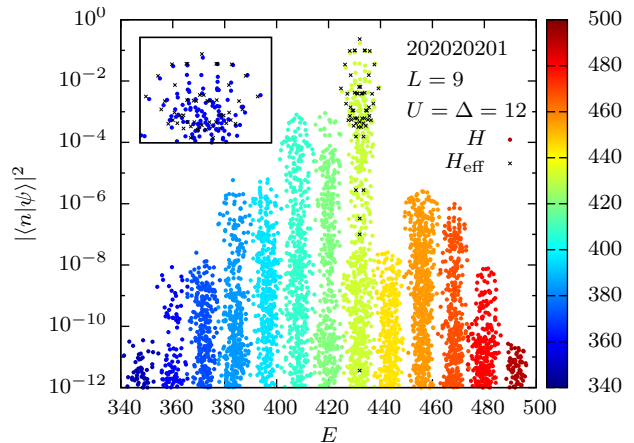


Figure S4. Overlap of the state 202020201 with the eigenstates of the tilted Bose-Hubbard model (S1) with $J = 1$ and $U = \Delta = 12$. The colors indicate the expectation value of the diagonal terms $\langle \hat{H}_U + \hat{H}_\Delta \rangle$ for each eigenstate. The black crosses correspond to the effective model (S4) (shifted by $E = \langle 202020201 | \hat{H} | 202020201 \rangle = 432$). The inset shows the top part of band with the highest overlap, where a band of $L = 9$ scarred eigenstates analogous to that in the PXP model can be seen.

As a side note, the system is also described by PXP-like effective models at other integer filling factors. The reviving initial states are of the form $|(n+1)(n-1)(n+1)(n-1)\dots(n+1)(n-1)n\rangle$ for $\nu = n$, e.g. $|3131\dots312\rangle$ for $\nu = 2$ and $|4242\dots423\rangle$ for $\nu = 3$, as shown in Fig. S5. Revival frequency increases with n as $\sqrt{n(n-1)}$, but the revivals decay faster for larger n .

GLOBAL VS. SINGLE-SITE FIDELITY

In this section we discuss the relation between two measures of similarity of pure states used in this work. One measure is the quantum fidelity

$$\mathcal{F}(|\phi\rangle, |\psi\rangle) = \|\phi\|\psi^2, \quad (\text{S11})$$

i.e., the global overlap between two pure states. This measure is very convenient for numerical simulations and theoretical analysis, but hard to measure in experiment. For this reason, we also consider a different measure consisting of an average of local measurements:

$$\mathcal{F}_{(r)}(|\phi\rangle, |\psi\rangle) = \frac{1}{L+1-r} \sum_{j=1}^{L+1-r} \text{Tr} \left[\hat{\rho}_{j,j+r-1}^\phi \hat{\rho}_{j,j+r-1}^\psi \right], \quad (\text{S12})$$

where $1 \leq r \leq L$ is the range of the measurements and

$$\hat{\rho}_{j,j+r-1}^\phi = \text{Tr}_{\perp, j, j+r-1} [|\phi\rangle\langle\phi|] \quad (\text{S13})$$

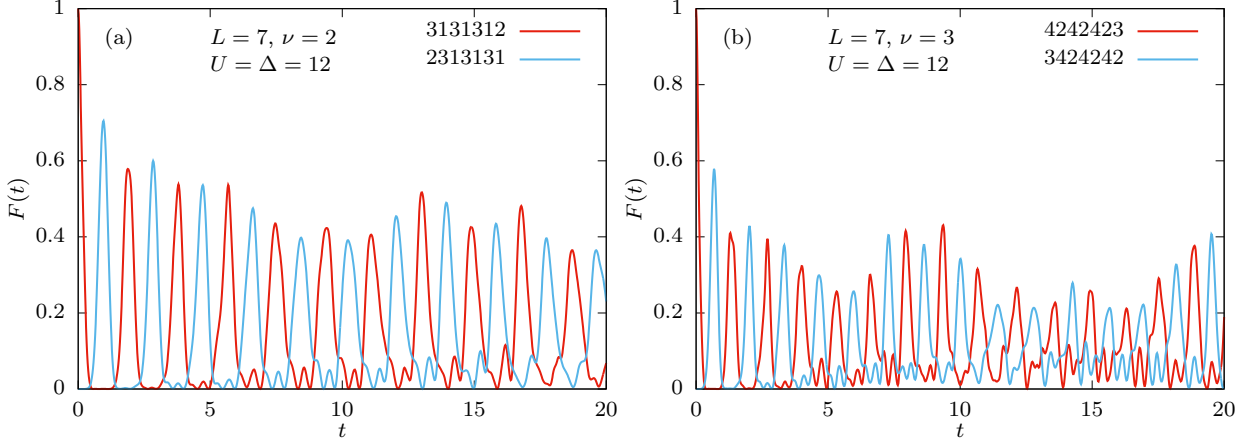


Figure S5. Evolution of quantum fidelity $F(t) = |\langle \psi_0 | e^{-iHt} | \psi_0 \rangle|^2$ starting from the Néel state $|\psi_0\rangle$ (red) and the amplitude of state transfer, $\mathcal{O}(t) = |\langle \psi | e^{-iHt} | \psi_0 \rangle|^2$, for the anti-Néel state $|\psi\rangle$ (blue). The evolution is governed by the tilted Bose-Hubbard Hamiltonian from Eq. (S1) with $J = 1$ and $U = \Delta = 12$. (a) Filling factor $\nu = 2$. (b) $\nu = 3$. The Hilbert space size is reduced by removing the configurations with more than 3 particles per site in (a) and more than 4 particles per site in (b).

is the density matrix obtained by performing the partial trace on all sites except sites $j - 1 + r$.

Both quantities, \mathcal{F} and $\mathcal{F}_{(r)}$, are real and obey

$$0 \leq \mathcal{F}(|\phi\rangle, |\psi\rangle), \mathcal{F}_{(r)}(|\phi\rangle, |\psi\rangle) \leq 1, \quad (\text{S14})$$

and

$$\mathcal{F}_{(r)}(|\phi\rangle, |\psi\rangle) = \mathcal{F}_{(r)}(|\psi\rangle, |\phi\rangle), \quad (\text{S15})$$

$$\mathcal{F}(|\phi\rangle, |\psi\rangle) = \mathcal{F}(|\psi\rangle, |\phi\rangle). \quad (\text{S16})$$

It is also important to note that

$$\begin{aligned} \mathcal{F}_{(L)}(|\phi\rangle, |\psi\rangle) &= \text{Tr} [|\phi\rangle \langle \phi | \psi\rangle \langle \psi |] \\ &= \|\phi\| \psi^2 = \mathcal{F}(|\phi\rangle, |\psi\rangle). \end{aligned} \quad (\text{S17})$$

While for arbitrary states $\mathcal{F}_{(r)}$ is neither an upper bound nor a lower bound of \mathcal{F} , it does not mean that this is never the case. We are now limiting our study to the case where the state ϕ is a product state. The consequence of that is that the reduced density matrix $\hat{\rho}_{j,j+r-1}^\phi$ will correspond to a pure state for any r . We can then choose a basis for each site such that $|\phi\rangle$ is a product of local basis states, and so a Fock basis state for the whole Hilbert space. Let us then denote the orthonormal states of this basis by $|\alpha\rangle$.

This allows us to rewrite the reduced density matrix as $\hat{\rho}_{j,j+r-1}^\phi = |\phi_{j,j+r-1}\rangle \langle \phi_{j,j+r-1}|$, where $|\phi_{j,j+r-1}\rangle$ corresponds to the state ϕ for sites j to $j + r - 1$ (remember that we can only do this because $|\phi\rangle$ is a product state).

This formulation implies the following simplification

$$\begin{aligned} \mathcal{F}_{(r)}(|\phi\rangle, |\psi\rangle) &= \frac{1}{L+1-r} \sum_{j=1}^{L+1-r} \text{Tr} \left[\hat{\rho}_{j,j+r-1}^\phi \hat{\rho}_{j,j+r-1}^\psi \right] \\ &= \frac{1}{L+1-r} \sum_{j=1}^{L+1-r} \text{Tr} \left[|\phi_{j,j+r-1}\rangle \langle \phi_{j,j+r-1}| \hat{\rho}_{j,j+r-1}^\psi \right] \\ &= \frac{1}{L+1-r} \sum_{j=1}^{L+1-r} \sum_{\substack{|\alpha\rangle \text{ s.t.} \\ \langle \alpha | \phi \rangle_{j,j+r-1} = 1}} \|\alpha\| \psi^2 \\ &= \frac{1}{L+1-r} \sum_{|\alpha\rangle} \|\alpha\| \psi^2 \sum_{j=1}^{L+1-r} \prod_{k=j}^{j+r-1} \langle \alpha_k | \phi_k \rangle \\ &= \|\phi\| \psi^2 + \frac{1}{L+1-r} \sum_{|\alpha\rangle \neq |\phi\rangle} \|\alpha\| \psi^2 \sum_{j=1}^{L+1-r} \prod_{k=j}^{j+r-1} \langle \alpha_k | \phi_k \rangle \\ &\geq \|\phi\| \psi^2 = \mathcal{F}(|\phi\rangle, |\psi\rangle), \end{aligned} \quad (\text{S18})$$

where $\langle \alpha | \phi \rangle_{j,j+r-1}$ denotes the product of $\langle \alpha_{j,j+1-r} \rangle$ and $\langle \phi_{j,j+1-r} \rangle$, which is always either 0 or 1. This means that $\|\alpha\| \psi^2$ contributes to $\mathcal{F}_{(r)}(|\phi\rangle, |\psi\rangle)$ with a weight of $\frac{1}{N+1-r}$ each time r consecutive sites are in the same state in $|\alpha\rangle$ and $|\phi\rangle$. This simple rule allows us to not only derive this inequality between \mathcal{F} and $\mathcal{F}_{(r)}$, but also to compare the effect of r on $\mathcal{F}_{(r)}$. Indeed, if with r a basis state $|\alpha\rangle$ has a weight of $\frac{n}{L+1-r}$, then if $n > 0$ with $r - 1$ it has a minimum weight of $\frac{n+1}{L+2-r}$. As $n \leq L+1-r$, it implies that $\frac{n}{L+1-r} \leq \frac{n+1}{L+2-r}$. If $n = 0$ then for $r - 1$ the same state cannot contribute less, and so for any n it contributes more or the same amount. Hence we can conclude that

$$\mathcal{F}_{(1)}(|\phi\rangle, |\psi\rangle) \geq \mathcal{F}_{(2)}(|\phi\rangle, |\psi\rangle) \geq \dots \mathcal{F}_{(L)}(|\phi\rangle, |\psi\rangle) = \mathcal{F}(|\phi\rangle, |\psi\rangle). \quad (\text{S19})$$

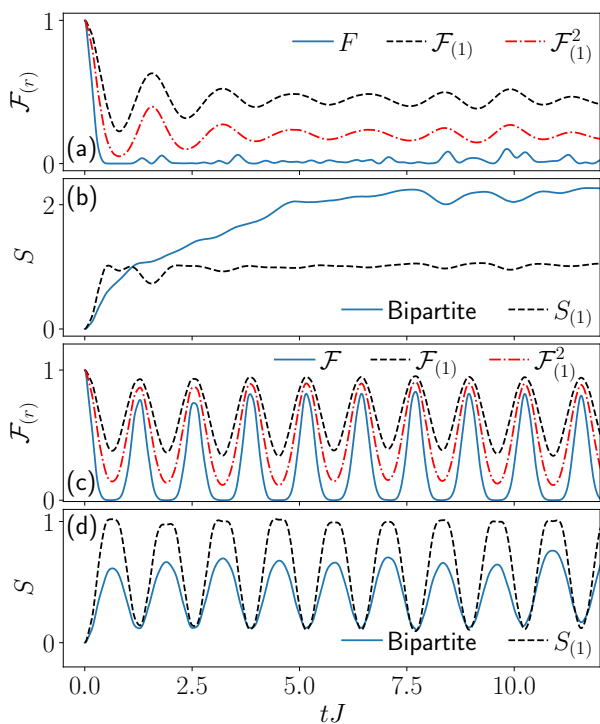


Figure S6. Comparison between global and local quantities for the polarized state (a)-(b) without and (c)-(d) with driving. Both the single-site fidelity and the single-site entropy effectively capture the behavior of their global counterpart. In both the undriven and driven cases, the squared single-site fidelity $\mathcal{F}_{(1)}^2$ provides a better approximation of \mathcal{F} than $\mathcal{F}_{(1)}$ while still acting as an upper bound. Tilted Bose-Hubbard model (S1), $J = 1$, $\Delta = U = 16$, $L = 11$, $L_A = 5$, driving parameters $U_0 = -2.38$, $U_m = 1.54$, $\omega = 4.90$.

Finally, it is important to note that the inequality $\frac{n}{L+1-r} \leq \frac{n+1}{L+2-r}$ is saturated if and only if $n = L + 1 - r$, meaning that $|\alpha\rangle$ and $|\phi\rangle$ are the same. This is important as $\mathcal{F}_{(r)}(|\phi\rangle, |\psi\rangle)$ is a weighted sum of all the $\|\alpha\|^2$ with weights equal or smaller to 1. In order for $\mathcal{F}_{(r)}(|\phi\rangle, |\psi\rangle)$ to be equal to $\mathcal{F}_{(r-1)}(|\phi\rangle, |\psi\rangle)$, all weights corresponding to a non-zero $|\langle\alpha|\psi\rangle|^2$ must stay the same. But the only weights that are not increasing are either the ones that stay equal to zero or the one of $|\alpha\rangle = |\phi\rangle$ which stays equal to one. This implies that *all* inequalities of Eq. S19 are simultaneously saturated if and only if $|\psi\rangle = |\phi\rangle$ (in which case they are all equal to one) or $\mathcal{F}_{(1)}(|\phi\rangle, |\psi\rangle) = 0$ (in that case they are all equal to 0). It is also possible for some of them to be saturated. This can only happen if any consecutive subset of length m of $|\phi\rangle$ and $|\psi\rangle$ are orthogonal, meaning the all $\mathcal{F}_{(r)}$ are equal to 0 for all $r \geq m$.

In the experimental setup we only have access to the single-site fidelity $\mathcal{F}_{(1)}$, which already mimics the behavior of the real fidelity \mathcal{F} (see Fig. S6). While it bounds \mathcal{F} from above, that bound is fairly loose. If we instead look at its square $\mathcal{F}_{(1)}^2$, we can see that it approximates \mathcal{F}

much better as it takes a lower value when \mathcal{F} is close to zero. While $\mathcal{F}_{(1)}^2$ is not guaranteed to be an upper bound of \mathcal{F} , our theoretical simulations indicate that it still effectively acts as one for the conditions we study. Our simulations also show that the single-site second Renyi entropy $S_{(1)}$ shows a very similar behavior to the bipartite half-chain second Renyi entropy S . While it is limited in the range of values it can take, $S_{(1)}$ is clearly able to distinguish between the two regimes we are seeing in our setup: rapid entropy growth until a plateau is reached, and very slow entropy growth with oscillations on top.

ALTERNATIVE MAPPING BETWEEN PXP AND TILTED 1D BOSE-HUBBARD WITH STAGGERED DETUNING

There is another mapping between the tilted 1D Bose-Hubbard and the PXP model which is based on the additional staggered potential term added to the the model in Eq. (S1):

$$\hat{H} = -J \sum_{i=1}^{L-1} (\hat{b}_i^\dagger \hat{b}_{i+1} + \hat{b}_{i+1}^\dagger \hat{b}_i) + \frac{U}{2} \sum_{i=1}^L \hat{n}_i (\hat{n}_i - 1) + \Delta \sum_{i=1}^L i \hat{n}_i + \frac{\delta}{2} \sum_{i=1}^L (-1)^{i-1} \hat{n}_i. \quad (\text{S20})$$

The parameter δ determines the energy offset between even and odd lattice sites. The odd ones are now “plus” sites where the δ term is positive, while the even one are “minus” sites where it is negative. This means that for an odd chain of length L there are $N = \frac{L-1}{2}$ minus sites and $N + 1 = \frac{L+1}{2}$ plus sites.

The model in Eq. (S20) has been experimentally studied (see [S10] and references therein). Its mapping to the U(1) quantum link model has been already established in the literature, as is the mapping between the U(1) quantum link model and the PXP model [S11]. However, the equivalence of the tilted Bose-Hubbard model with staggered detuning and the PXP model was to our knowledge never explicitly stated, so we will briefly explain it here. This mapping is valid in the regime $U \approx 2\delta \gg J$ and at filling factor $\nu = 1/2$.

When $U \approx 2\delta \gg J$, the second-order process $101 \leftrightarrow 020$ becomes resonant. Nonzero tilt Δ makes other relevant second-order processes such as $100 \leftrightarrow 001$ off-resonant. In this regime and for odd system size L with filling factor $\nu = \frac{L+1}{2L}$, the effective Hamiltonian at second order of the model in Eq. (S20) is fragmented. One of these fragments can be mapped to the PXP model up to some diagonal boundary terms. To find the corresponding state in PXP, one only needs to look at the “minus” sites. Doublons on these sites are mapped to PXP excitations, as the resonant processes cannot create two doublons on two adjacent minus sites. Due to

the nature of the resonant process they can never be singly-occupied, and empty minus sites are mapped to non-excited atoms. This means that the corresponding PXP model has length $N = \frac{L-1}{2}$, which is just the number of minus sites.

The Néel states $\bullet\bullet\circ\circ\dots\circ\circ$ and $\circ\circ\bullet\bullet\dots\bullet\bullet$ are then mapped to $02000200\dots02001$ and $100200020\dots0020$ respectively, while $101010\dots101$ corresponds to the fully polarized state $\circ\circ\circ\dots\circ\circ\circ$.

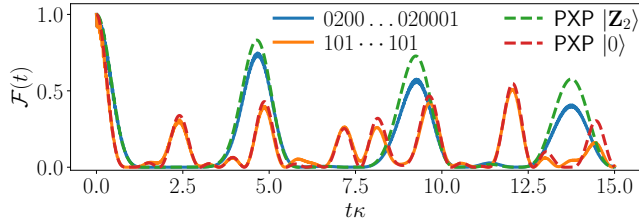


Figure S7. Time evolution of the fidelity for tilted Bose-Hubbard model with staggered detuning with $L = 13$, $U = 2\delta = 120$, $J = 1$ and $\Delta = 43.3$, and for the PXP model with $N = 6$. The constant κ is the effective hopping strength in each model (see text).

Fig. S7 shows the wave function fidelity over time for the model in Eq. (S20) with $U=2\delta > \Delta \gg J$, and for the PXP model it can be mapped to. To directly compare the two models, we have rescaled the time axis by the constant κ , which takes the value $\sqrt{2}J^{(2)} = \sqrt{2} \times 4J^2U/(U^2-4\Delta^2)$ in the Bose-Hubbard model and Ω in the PXP model. The staggered Bose-Hubbard model oscillates between two product states, $02000200\dots02001$ and $100200020\dots0020$, which are the analogs of the Néel states in the PXP model. Overall, the dynamics is seen to be very similar in the two models, with the slight difference between the two being likely due to the boundary terms defined in Eq. (S21) below.

To derive the mapping to the PXP model rigorously, we can separate the Hamiltonian in Eq. (S20) as $\hat{H} = \hat{H}_0 - J\hat{V}$ and perform the Schrieffer-Wolff transformation [S7]. Here \hat{H}_0 encompasses all the diagonal terms while V simply corresponds to hopping, which assumes that $\delta, \Delta, U \gg J$. Furthermore, we will only focus on the regime $U = 2\delta$, in which case there are no first order terms. If U is close but not equal to 2δ , then the effective Hamiltonian at first order will contain diagonal terms proportional to $|U - 2\delta|$. Finally, we only focus on the connected component of the second order Hamiltonian that can be mapped to the PXP model, meaning that resonant processes like $02010 \leftrightarrow 11001$ are ignored as these configuration cannot appear in the Hilbert space component of interest.

In the relevant part of the Hilbert space, the only off-diagonal resonant process at second order is $101 \leftrightarrow 020$, which appears with a weight of $\sqrt{2}J^{(2)}$, where $J^{(2)} = \frac{4J^2U}{U^2-4\Delta^2}$. There are also two allowed second-order di-

agonal processes in the bulk of the chain: $010 \leftrightarrow 010$ and $020 \leftrightarrow 020$. They have a respective weight of $J^{(2)}$ and $2J^{(2)}$. However, as creating a new doublon means emptying two singly-occupied sites, the diagonal matrix elements do not change under the off-diagonal process. The only exception to this is hopping at the boundaries of the chain. For the leftmost site, only hopping to the right and then back is possible, leading to a contribution of $\frac{2J^2}{U-2\Delta}$ instead of $J^{(2)}$. For the rightmost site only hopping to the left is possible and the contribution is $\frac{2J^2}{U+2\Delta}$. This means that not all diagonal matrix elements are the same but they vary between $J^{(2)}N = \frac{L-1}{2}J^{(2)}$ and $(N+1)J^{(2)} = \frac{L+1}{2}J^{(2)}$. However the differences between the diagonal elements are $\mathcal{O}(1)$ and do not scale with L , so they become negligible for large system sizes. All together, the second order Hamiltonian can be mapped to the following model.

$$\hat{H}_{\text{eff},2} = J^{(2)}N + \sqrt{2}J^{(2)} \left[\hat{X}_1\hat{P}_2 + \hat{P}_{N-1}\hat{X}_N + \sum_{j=2}^{N-1} \hat{P}_{j-1}\hat{X}_j\hat{P}_{j+1} \right] + \frac{2J^2}{U+2\Delta}\hat{n}_1 + \frac{2J^2}{U-2\Delta}\hat{n}_N, \quad (\text{S21})$$

with $J^{(2)} = \frac{4J^2U}{U^2-4\Delta^2}$, $N = \frac{L-1}{2}$, $\hat{n}_j = \frac{1+Z_j}{2}$, where Z denotes the usual Pauli z matrix [\hat{P}_j and \hat{X}_j were defined previously below Eq. (S5)]. It is worth mentioning that for $U = 2\delta$, the third order effective Hamiltonian is identically zero due to the absence of diagonal elements in the perturbation V (which is simply the hopping) and the next correction only happens at fourth order.

EFFECT OF PERIODIC DRIVING ON \mathbb{Z}_2 SCARS

In this section we numerically explore the effect of driving on the stabilization of many-body scars and revival dynamics, both in the PXP and tilted Bose-Hubbard models.

Driven PXP model

Periodic driving has been shown to enhance and stabilize the revivals in the PXP model [S12, S13]. The optimal driving frequency was found to be close to twice that of revivals in the pure PXP model without driving. We consider the following spatially-uniform cosine driving scheme which was also experimentally implemented in Ref. [S12]

$$\hat{H}(t) = \sum_i \left(\Omega\hat{P}_{i-1}\hat{X}_i\hat{P}_{i+1} - \mu(t)\hat{n}_i \right), \quad (\text{S22})$$

$$\mu(t) = \mu_0 + \mu_m \cos(\omega t). \quad (\text{S23})$$

Here, μ_0 is the static detuning, μ_m modulation amplitude and ω driving frequency. For simplicity, when work-

ing with the PXP model, we impose periodic boundary conditions (PBC). We determine the optimal values of μ_0 and μ_m by scanning the parameter space for the highest time-averaged fidelity. To make sure we found the globally-optimal values of the driving parameters, we have also checked the results against the simulated annealing algorithm implemented in GNU Scientific Library.

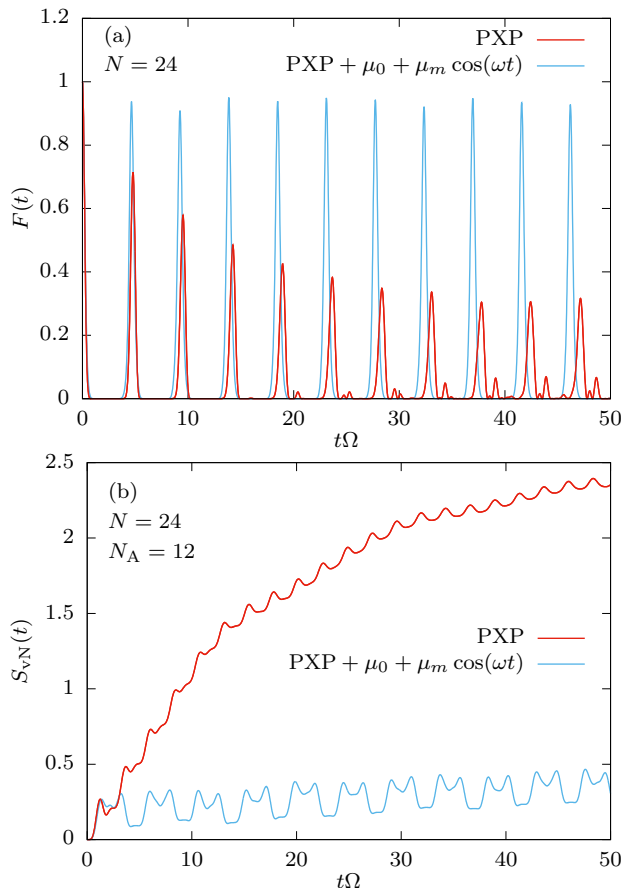


Figure S8. Comparison of dynamics in the pure (red), and periodically driven PXP model (blue). System size $N = 24$, driving parameters $\mu_0/\Omega = 1.15$, $\mu_m/\Omega = 2.67$, $\omega/\Omega = 2.72$. (a) Fidelity. (b) Entanglement entropy for $N_A = 12$.

The evolution of quantum fidelity starting from the Néel state $|\mathbb{Z}_2\rangle = |\bullet\circ\bullet\circ\bullet\circ\dots\rangle$ can be seen in Fig. S8(a), both without driving (red) and driven with optimal driving parameters $\mu_0/\Omega = 1.15$, $\mu_m/\Omega = 2.67$ and $\omega/\Omega = 2.72$ (blue). Driving leads to high revivals whose amplitude remains close to 1 over very long times. Additionally, the driving also strongly suppresses the growth of entanglement entropy, as can be observed in Fig. S8(b).

In order to understand the mechanism of revival enhancement, in Fig. S9 we show the effects of periodic driving on the trajectory in the Hilbert space. The x and y axes in this figure are the expected numbers of excitations on the even and odd sublattice (normalized by the maximal number of excitations $n_{\max} = N/2$), $\langle\hat{n}_A\rangle$

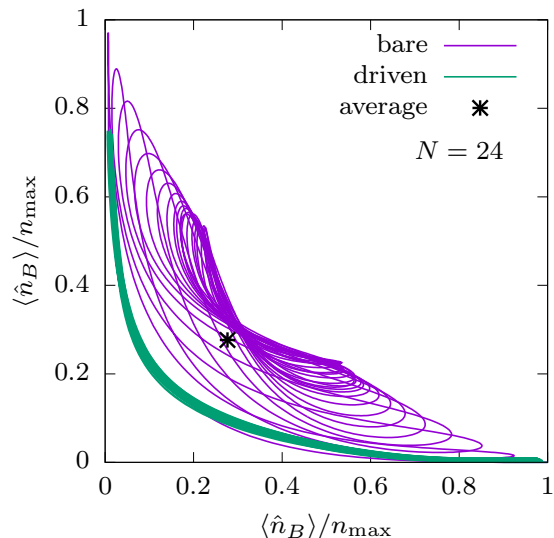


Figure S9. Trajectory in the Hilbert space, represented by the the expected numbers of excitations on the even and odd sublattices, $\langle\hat{n}_A\rangle$ and $\langle\hat{n}_B\rangle$, normalized by the maximal number of excitations $\hat{n}_{\max} = N/2$. Purple: no driving, $\mu(t) = 0$. The trajectory at first keeps returning to the vicinity of the Néel states, but then slowly relaxes towards the average value of $\langle\hat{n}_A\rangle$ and $\langle\hat{n}_B\rangle$. Green: driving with optimal parameters $\mu_0/\Omega = 1.15$, $\mu_m/\Omega = 2.67$ and $\omega/\Omega = 2.72$, results in dynamics that sharply concentrates around the trajectory and avoids thermalization.

and $\langle\hat{n}_B\rangle$ respectively. The two Néel states are located in the bottom right and top left corner of Fig. S9, while the polarized state $|\circ\circ\circ\dots\rangle$ is in the bottom left corner. The states on the main diagonal (except the Néel states) and in the triangle above it are forbidden due to the PXP constraints.

In the undriven case (purple), the trajectory at first oscillates between the Néel and anti-Néel states in the corners, while passing through a region with a lower number of excitations (bottom left). However, as the time progresses, the wavefunction starts to thermalize and the trajectory drifts towards towards the average numbers of excitations $(\langle\hat{n}_A\rangle, \langle\hat{n}_B\rangle) = (0.276, 0.276)$. When the driving is turned on (green), the trajectory continues to approximately repeat the first revival period in the undriven case and does not seem to thermalize even at very late times. In this way the revivals are stabilized and enhanced. Another effect of driving is that the overlap with the anti-Néel state is now lower, but its peaks do not decay with time.

Finally, in Fig. S10 we studied the Floquet modes of the driven PXP model. The Floquet modes are a generalization of eigenstates for periodic time-dependent Hamiltonians $\hat{H}(t + \frac{2\pi}{\omega}) = \hat{H}(t)$. Unlike the eigenstates, the Floquet modes evolve in time, but they are time-periodic with the same periodicity as the driven Hamiltonian, $\Phi_n(t + \frac{2\pi}{\omega}) = \Phi_n(t)$. We have computed all the

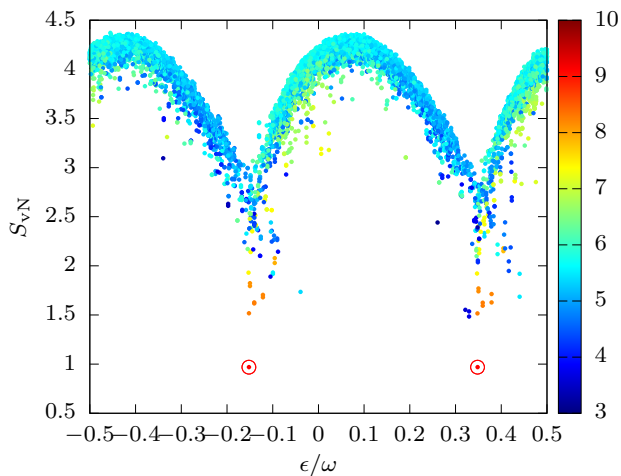


Figure S10. Bipartite von Neumann entanglement entropies of all Floquet modes for the driven PXP model with driving parameters $\mu_0/\Omega = 1.15$, $\mu_m/\Omega = 2.67$ and $\omega/\Omega = 2.72$. System size $N = 20$, subsystem $N_A = 10$. The colour scale represents the expectation value of the total number of excitations for each mode. The two Floquet modes which have the highest overlap with the Néel state are encircled in red. They have the lowest entanglement entropy and the highest number of excitations and their quasienergies are separated by $\omega/2$.

Floquet modes $\Phi_n(t=0)$ for the driven case by numerically constructing the evolution operator over one period $T = \frac{2\pi}{\omega}$, $\hat{U}(T)$, and diagonalizing it.

In Fig. S10 we plot the bipartite von Neumann entanglement entropies of all the Floquet modes for the optimal driving parameters. There are two symmetric ‘arcs’ in the entropy plot, which suggests that the Floquet Hamiltonian might be fractured into two components. The expected numbers of excitations for each mode are represented by different colours. The two lowest entropy modes have the highest overlap with the Néel state $|\mathbb{Z}_2\rangle$. One of them is approximately $\Phi_1(0) = (|\mathbb{Z}_2\rangle + |\mathbb{Z}'_2\rangle)/\sqrt{2}$ and the other is close to $\Phi_2(0) = (|\mathbb{Z}_2\rangle - |\mathbb{Z}'_2\rangle)/\sqrt{2}$, while the quasienergy separation between them is $\Delta\epsilon = \epsilon_1 - \epsilon_2 \approx \omega/2$. This provides a simple explanation for the revival dynamics starting from the Néel state, as will be outlined below.

Let us assume that the two idealized states $\Phi_1(0)$ and $\Phi_2(0)$ are indeed Floquet modes. The initial state $|\mathbb{Z}_2\rangle$ will then be a superposition of only these two modes

$$\psi(0) = \frac{1}{\sqrt{2}}\Phi_1(0) + \frac{1}{\sqrt{2}}\Phi_2(0) \quad (\text{S24})$$

and will evolve as

$$\begin{aligned} \psi(t) &= \frac{1}{\sqrt{2}}e^{-i\epsilon_1 t}\Phi_1(t) + \frac{1}{\sqrt{2}}e^{-i\epsilon_2 t}\Phi_2(t) = \\ &= \frac{1}{\sqrt{2}}e^{-i\epsilon_1 t}(\Phi_1(t)) + e^{i\Delta\epsilon t}\Phi_2(t). \end{aligned} \quad (\text{S25})$$

After one driving period, the two Floquet modes will return to their initial states, but the relative phase will be $e^{i\frac{\epsilon_2}{\omega}2\pi} = e^{i\pi} = -1$. The wavefunction after one period will therefore be in the anti-Néel state (with an unimportant phase prefactor), $\psi(T) = e^{-i\epsilon_1 T}|\mathbb{Z}'_2\rangle$. It will take two driving periods for the relative phase to again become $+1$ and the wavefunction to return to the initial $|\mathbb{Z}_2\rangle$ state. This is the origin of the period doubling (subharmonic response to periodic driving) which was observed in previous works [S12].

We note that the period doubling will disappear if we resolve the translation symmetry and work only in the $k = 0$ momentum subspace. The initial state $(|\mathbb{Z}_2\rangle + |\mathbb{Z}'_2\rangle)/\sqrt{2}$ will in that case have high overlap with only a single Floquet mode and will trivially oscillate with the same frequency as the periodic drive.

Driving the tilted 1D Bose-Hubbard model

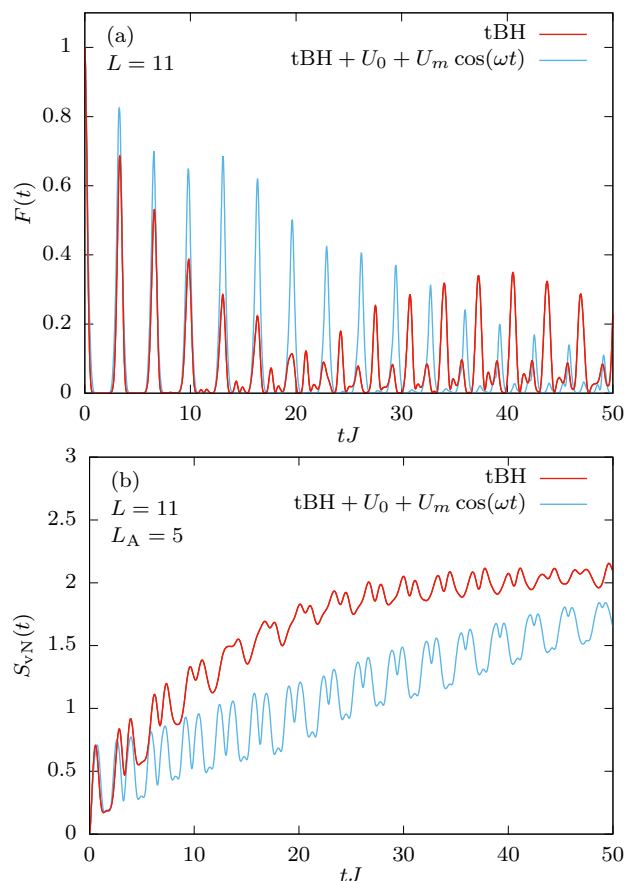


Figure S11. Comparison of the dynamics in the tilted Bose-Hubbard model without (red) and with periodic driving (blue). System size $L = 11$, maximally 3 particles per site, $J = 1$, $\Delta = 16$, driving parameters $U_0 = 1.85$, $U_m = 3.71$, $\omega = 3.85$. (a) Fidelity. (b) Entanglement entropy for subsystem size $L_A = 5$ sites.

As the tilted Bose-Hubbard model can be mapped to the PXP model in the $U \approx \Delta \gg J$ limit, see Section , we also expect to be able to enhance many-body scarring via periodic modulation of the term corresponding to the number of excitations. In the Bose-Hubbard case, such a term is conveniently provided by the on-site interaction strength U . However, we cannot use periodic boundary conditions due to the linear tilt which would be discontinuous at the boundary. We therefore consider the Bose-Hubbard model with open boundary conditions and periodically modulate the interaction strength $U(t)$:

$$\hat{H}(t) = -J \sum_{i=1}^{L-1} (\hat{b}_i^\dagger \hat{b}_{i+1} + \hat{b}_{i+1}^\dagger \hat{b}_i) + \frac{U(t)}{2} \sum_{i=1}^L \hat{n}_i (\hat{n}_i - 1) + \Delta \sum_{i=1}^L i \hat{n}_i, \quad (\text{S26})$$

with the driving given by

$$U(t) = \Delta + U_0 + U_m \cos(\omega t). \quad (\text{S27})$$

The driving parameters, U_0 , U_m and ω , are the static detuning and the modulation amplitude of the interaction strength and the driving frequency, respectively.

The modulation of interaction strength indeed leads to enhanced revivals in the Bose-Hubbard model, see Fig. S11. In particular, the slope of entanglement growth is significantly reduced, with scarred oscillations becoming more pronounced. However, in local observables, such as the density of doublons, the effects of driving are less striking than in the pure PXP model. The reason for more modest enhancement of revivals in the Bose-Hubbard model is the competition between stabilization of revivals within the PXP subspace and the processes which destroy the mapping to PXP model, such as the terms creating 3 or more bosons on a site. Additionally, the optimal driving parameters are not the same as those for the PXP model (up to the trivial rescaling by $\Omega = \sqrt{2}J$ to match the normalization of off-diagonal matrix elements). Increasing the tilt parameter Δ brings the tilted Bose-Hubbard model closer to the PXP model, but it is still necessary to perform a separate optimization of driving parameters.

QUANTUM MANY-BODY SCARS IN THE POLARIZED STATE

In the main text we reported the observation of many-body scarring associated with the state that contains no doublons, $|111\dots\rangle$, or equivalently the fully-polarized state $|\circ\circ\circ\dots\rangle$ in the PXP model. In this section we provide extensive theoretical evidence for many-body scarring in the polarized state. While the polarized state does not exhibit many-body scarring in the pure PXP model,

consistent with previous work [S14], it does display weak signatures of non-ergodicity in local observables for sufficiently small systems. In this section, we show that static detuning and its periodic modulation can be used to stabilize the scarring from this initial state. As we will demonstrate below, the many-body scarring in the polarized state is distinct from the previously studied ‘‘dynamical freezing’’ regime associated with $|\circ\circ\circ\dots\rangle$ state in the PXP model driven by a square pulse protocol [S15].

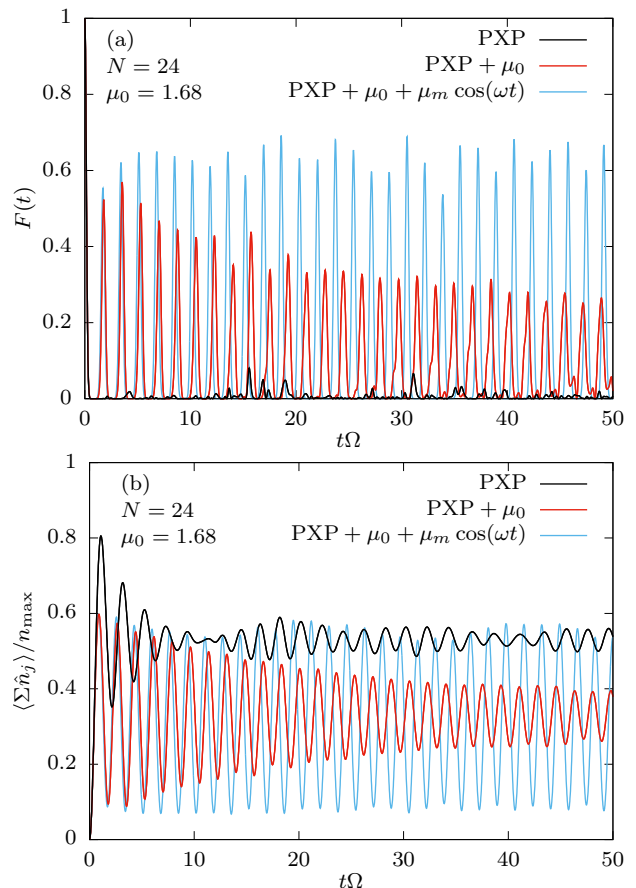


Figure S12. Comparison of dynamics from the polarized state in the pure PXP model (black), with static detuning only (red), and with both static detuning and periodic driving (blue). System size $N = 24$, driving parameters $\mu_0/\Omega = 1.68$, $\mu_m/\Omega = -0.50$, $\omega/\Omega = 3.71$. (a) Fidelity. (b) Expected total number of excitations normalized by the maximal number of excitations $n_{\max} = N/2$.

Pure PXP model

The polarized state $|\circ\circ\circ\dots\rangle$ is expected to thermalize in the pure PXP model. Nevertheless, the state exhibits some signatures of non-ergodic dynamics in smaller system sizes, such as oscillations in the expectation values of certain local observables. For example, as shown by the black lines in Figs. S12(a) and (b), even though there

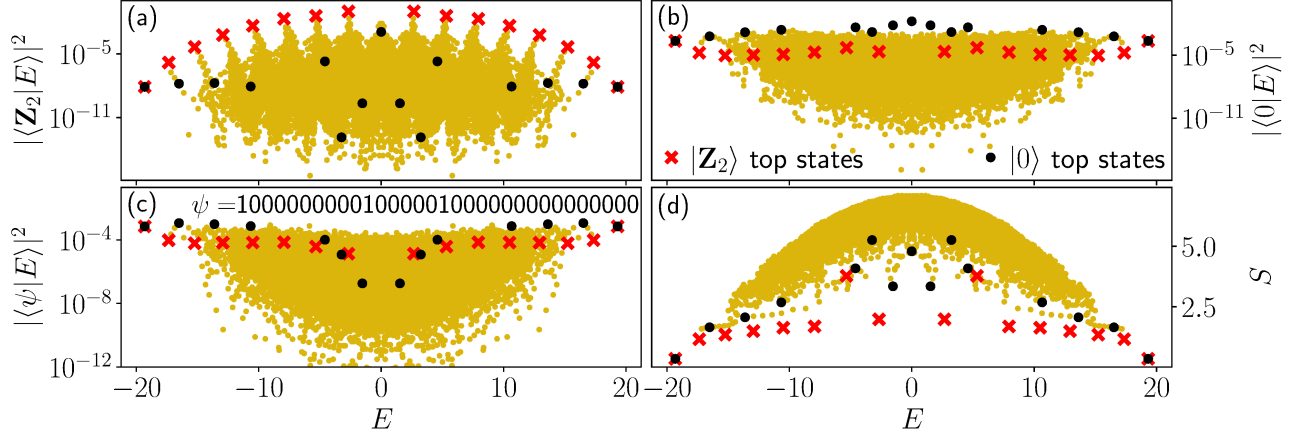


Figure S13. PXP eigenstates, system size $N = 32$, symmetry sector $\{k = 0, p = 1\}$. Overlap with (a) Néel state. (b) polarized state. (c) randomly chosen state. (d) Bipartite entanglement entropies of all eigenstates. The highest-overlap eigenstates in their energy window are marked by red crosses for the Néel state and by black dots for the polarized state.

are no significant revivals in wave function fidelity, some oscillations in the number of excitations are still visible.

A closer look at the eigenstates of the PXP Hamiltonian and their overlap with the polarized state reveals the underlying reason for this behaviour, see Fig. S13. In Fig. S13(a) we plot the overlap of all PXP eigenstates with the Néel state, showing the well known band [S5] of scarred eigenstates marked by the red crosses and corresponding tower structures. In contrast, there is no such band of high-overlap eigenstates for a randomly chosen state, see Fig. S13(c). The polarized state is between these two cases, as can be observed in Fig. S13(b). Although there is no well defined band of scarred eigenstates as for the Néel state, there is still a number of unusually high-overlap eigenstates which are marked by the black dots. Finally, in Fig. S13(d) we show the entanglement entropies of all eigenstates. The lowest-entropy eigenstates are the Néel state scars (red crosses), but the eigenstates with the highest overlap with the polarized state (black dots) also have lower than average entanglement entropies. Thus, we conclude that the polarized state is poised to develop many-body scarring by a suitable perturbation of the PXP model. We next show that this can be achieved by applying static detuning.

Static detuning in the PXP model

The addition of a static detuning term

$$\hat{H}(\mu_0) = \hat{H}_{\text{PXP}} + \mu_0 \sum_j \hat{n}_j \quad (\text{S28})$$

results in the appearance of a band of atypical eigenstates with high overlap with the polarized state, as can be observed in Fig. S14. The band is still not well separated from the bulk at lower values of μ_0/Ω , see Figs. S14(a)

and (b). At larger values of μ_0/Ω , the energy spectrum starts to split into disconnected bands, as shown in Fig. S14(d). We are interested in the intermediate regime shown in Fig. S14(c), $\mu_0/\Omega \approx 1.68$, where there is a clearly visible band of scarred states, but the bulk of the energy spectrum is still continuous.

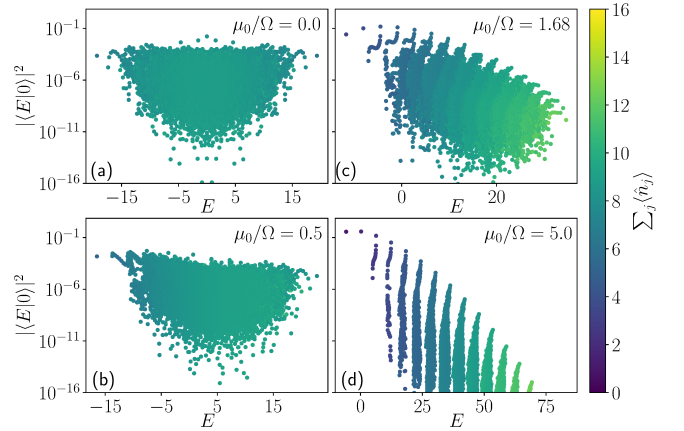


Figure S14. Overlap between the polarised state and the PXP eigenstates in the symmetry sector $\{k = 0, p = 1\}$ for $N = 32$. Each subfigure corresponds to a different value of the static detuning, and the color indicates the expectation value of the number of excitations for each eigenstate.

In addition to having the highest overlap with the polarized state, the special states are also approximately equidistant in energy and have lower entanglement entropy than most other eigenstates. These are all paradigmatic properties of quantum many-body scars. However, one striking difference compared to the Néel state scars is that the highest-overlap states are not concentrated in the middle of the spectrum. Instead, most of them are located at one edge of the energy spectrum, but the

band of atypical states still continues well into the higher energy densities, see Fig. S14(c). The fact that special eigenstates are biased towards one end of the spectrum is expected since the detuning potential breaks the particle-hole symmetry of the PXP Hamiltonian [S6].

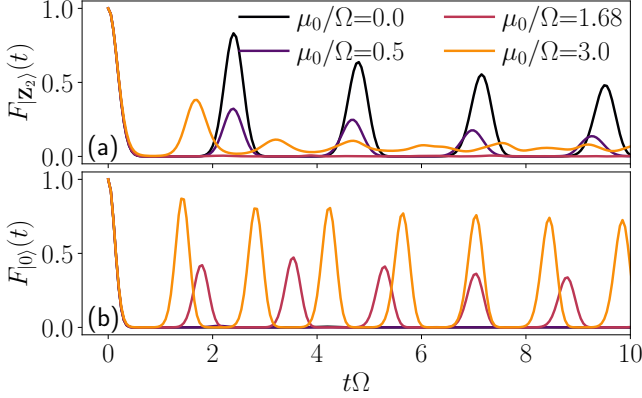


Figure S15. Revival fidelity for the Néel and polarised states in the symmetry sector $\{k = 0, p = 1\}$ for $N = 32$. (a) Néel state. (b) polarised state. At low detuning only the Néel states revives while in for $\mu_0/\Omega \gg 1$ both states do. However in the intermediate regime $\mu_0/\Omega \approx 1$ only the polarised states has revivals while the Néel state thermalises like the other product states.

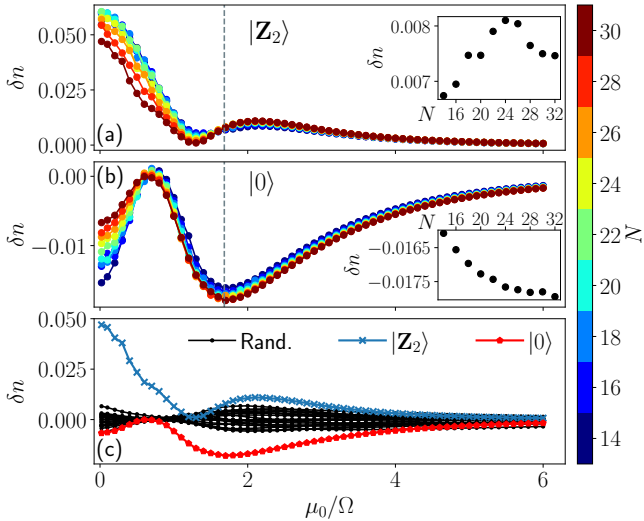


Figure S16. Difference of expectation value between the diagonal and canonical ensemble for the operator $\frac{1}{N} \sum_j \hat{n}_j$ in the PXP model. (a) Néel state. (b) polarised state. (c) comparison of different states for $N = 30$. The color scale in (a) and (b) corresponds to the system size N , while the insets show the results for various N with μ_0/Ω fixed to 1.68 (along the grey dashed line).

This emergence of scarred eigenstates significantly affects the revival dynamics, as illustrated in Figs. S12 and S15. For the Néel state in Fig. S15(a), the detuning

monotonically destroys the revival, until we reach the regime of very large detuning $\mu_0 \gtrsim 3$ which places the Néel state in its own fragment of the Hilbert space. By contrast, for the polarized state in Fig. S15(b) we see the revivals start to emerge at moderate detuning $\mu_0/\Omega \approx 1$. The frequency of the revival is found to match the energy separation between the scarred states in Fig. S14(c). The oscillations in the number of excitations are also enhanced and their frequency has changed to the frequency of fidelity revivals. This is the regime that corresponds to the many-body scarring observed in experiment. We note that the revivals from the polarized state also persist in the trivial large-detuning limit ($\mu_0 \gtrsim 3$) where the polarized state is effectively in its own fragment of the Hilbert space, similar to the Néel state.

The addition of detuning not only affects the short-time dynamics, but also *infinite-time* expectation values. After a quench, the value of any observable will reach the value predicted by the diagonal ensemble $O_d = \sum_{i,j} O_{i,j} \delta_{i,j} c_j c_i^*$, where $O_{i,j} = \langle E_i | O | E_j \rangle$ and $c_i = \langle E_i | 0 \rangle$. However we also expect the observable to thermalize towards the value predicted by the canonical ensemble $O_{th} = \text{Tr} [\hat{\rho}_{th} \hat{O}]$, where $\hat{\rho}_{th} = \frac{1}{Z} e^{-\beta \hat{H}}$ with $Z = \text{Tr} [e^{-\beta \hat{H}}]$ and β the inverse temperature. Note that we also restrict \hat{H} to the symmetry sector invariant under translation and spatial inversion as it is the only one compatible with the $|0\rangle$ state. A large difference between the predictions of these two ensembles for a given initial state is an indicator of the violation of the Eigenstate Thermalization Hypothesis [S16, S17]. For the PXP model we will use the operator $\hat{n} = \frac{1}{N} \sum_j \hat{n}_j$, which counts the average number of excitations in the system [S18], and denote the difference between the ensemble predictions by δn . The Néel state is most athermal at zero detuning, while the peak for the polarised state occurs around $\mu_0/\Omega = 1.7$, see Fig. S16. For larger values of the detuning these two states become respectively the topmost and ground states, meaning that the temperature is $\pm\infty$ and both ensembles agree exactly.

Periodic driving in the PXP model

Finally, in order to stabilize revival and many-body scarring in the polarized state at *late* times, we need to modulate the detuning amplitude, in addition to the static detuning. Using the same driving protocol as for the Néel state in Eq. (S23), we can enhance and stabilize the revivals from the polarized state at late times – see Fig. S12 (blue lines). The optimal driving frequency is found to be close to the frequency of revivals in the undriven case with static detuning.

In Fig. S17 we plot the entanglement energies of all the Floquet modes $\Phi_n(t = 0)$ for the optimal driving parameters. As in Fig. S10, the colour scale represents

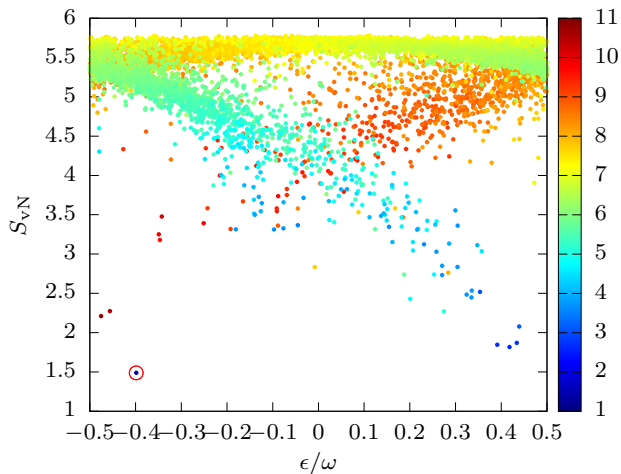


Figure S17. Bipartite von Neumann entanglement entropies of all Floquet modes for $\mu_0/\Omega = 1.68$, $\mu_m/\Omega = -0.50$ and $\omega/\Omega = 3.71$. System size $N = 26$, subsystem $N_A = 13$, symmetry sector $k = 0$. The colour scale represents the expectation value of the total number of excitations for each state. The Floquet mode with the highest overlap with the polarized state is encircled in red. This mode has the lowest entanglement entropy and the lowest number of excitations.

the expected number of excitations for each mode. The translational symmetry is now resolved and we show only the modes inside the $k = 0$ momentum subspace. There is a single mode that has high overlap with the polarized state, which explains the revival dynamics in Figs. S12 and S15(b). Note that there is no period doubling in this case.

Detuning and periodic driving in the tilted Bose-Hubbard model

Finally, we confirm that our conclusions about many-body scarring associated with the polarized state also hold in the full tilted Bose-Hubbard model in the regime $U \approx \Delta$, where we expect the effective description to be close to the PXP model. We will show that the driving leads to a strong suppression of entanglement growth and makes off-resonant the processes that cause leakage out of the PXP subspace.

In Fig. S18 we compare the dynamics at the resonance $U = \Delta$ (black lines, corresponding to the pure PXP model), at $U = \Delta + U_0$ (red lines, corresponding to the PXP model with static detuning), and for $U(t) = \Delta + U_0 + U_m \cos(\omega t)$ (blue lines, corresponding to the periodically driven PXP model). Due to the very fast growth of the Hilbert space size, we restrict the maximal number of bosons per site to 3. The results are consistent with those for the PXP model shown in Fig. S12. Note that the frequency of fidelity revivals in Fig. S18(a) is the frequency of PXP revivals multiplied by a factor of

$\sqrt{2}$ which comes from the off-diagonal matrix elements in the Bose-Hubbard model. The expected number of doublons, which is related to the number of PXP excitations is shown in Fig. S18(b).

The growth of entanglement entropy is suppressed by the addition of static detuning and even more by periodic driving, see Fig. S18(c). There are two factors that contribute to this behaviour. One is the dynamics inside the PXP subspace. The other is related to the leakage out of this subspace, which is represented by the number of sites with 3 particles in Fig. S18(d). The static detuning by itself significantly decreases this quantity, while the periodic driving does not seem to result in a substantial further improvement for the polarized state.

OTHER QUANTUM MANY-BODY SCARRED STATES

In addition to the Néel state and the polarized state, we also find other initial states which revive in the PXP model with static detuning, Eq. (S28). These initial states are the ground states of $\hat{H}(\mu_i)$ and they exhibit revivals when the detuning is quenched to a different value, $\hat{H}(\mu_i) \rightarrow \hat{H}(\mu_f)$. This setup generalizes the quench protocols studied in the main text. For example, setting $\mu_i \rightarrow -\infty$, the ground state is simply the Néel state and then quenching to $\mu_f = 0$ (pure PXP model) leads to the appearance of \mathbb{Z}_2 quantum many-body scars. Similarly, if we set $\mu_i \rightarrow \infty$ then the ground state is the $|0\rangle$ state and quenching to $\mu_f = 1.68\Omega$ also leads to scarring, as shown in the main text.

However, we observe similar scarring phenomenology in a larger set of initial conditions by varying the parameters μ_i and μ_f . Unlike the Néel state and the polarized state, the ground states of $\hat{H}(\mu_i)$ are far from product states for $|\mu_i| < 2$. However, they also have low entanglement and can be prepared experimentally. In Fig. S19 we illustrate this with an example for $\mu_i = -0.76\Omega$ and $\mu_f = 1.6\Omega$. For this set of parameters, we recover a similar scarring phenomenology as shown in the main text for the polarized state with $\mu_0 = 1.68$. However, we stress that the initial state considered here, i.e., the ground state of $\hat{H}(\mu_i)$, is now far from both the Néel and polarized states (the overlap with these states is on the order 10^{-5}). We emphasize that these values of μ are not fine tuned, and we find large regions of μ_i and μ_f leading to scarring.

In Fig. S19 (a) we recover a dynamics close to what could be observed for the polarized state with $\mu = 1.68\Omega$. During the evolution, the state periodically transfers to the polarized state and then returns to itself. The frequency of revivals is approximately the same as that for the polarized state evolved with the same static detuning μ_f , but the revivals are more prominent. The overlap of the $\hat{H}(\mu_i)$ ground state with all the eigenstates of $\hat{H}(\mu_f)$

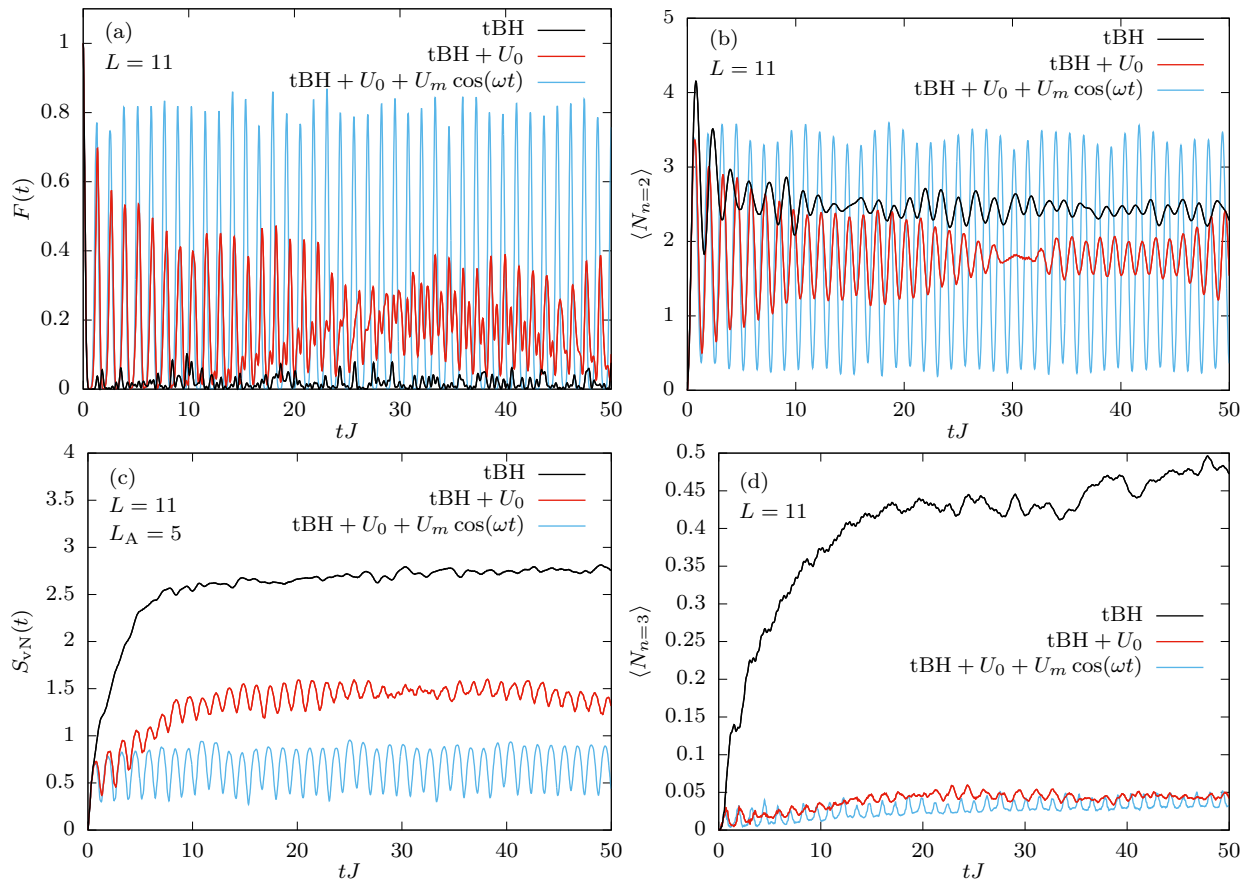


Figure S18. Comparison of dynamics in the tilted Bose-Hubbard model (black), with static detuning only (red), and with both static detuning and periodic driving (blue). System size $L = 11$, maximally 3 particles per site, $J = 1$, $\Delta = 16$, driving parameters $U_0 = -2.38$, $U_m = 1.54$, $\omega = 4.90$. (a) Fidelity. (b) Expected total number of doublons $N_{n=2}$. (c) Entanglement entropy for subsystem size $L_A = 5$. (d) Expected total number of sites with three particles $N_{n=3}$ (indicates the leakage from the PXP subspace).

is shown in Fig. S19(b). Comparing with the top states having overlap with the polarized state at the same value μ_f (red crosses) we see a similar pattern. More than that, the same atypical eigenstates have a high overlap for both states, but the phase is different in the two cases. This is similar to what is observed with the Néel state and its translated version for $\mu_f=0$. Both have the same overlap magnitude with each eigenstate, but the phases are different.

EFFECT OF DETUNING ON THE SPECTRAL STATISTICS OF THE PXP MODEL

In this section we show that the addition of finite detuning to the PXP model does not make this model integrable. We study the energy level spacings $s_n = E_{n+1} - E_n$, which we normalize to have $\langle s_n \rangle = 1$. For an integrable model, $\{s_n\}$ should follow the Poisson distribution, while for a chaotic model we expect to see the Wigner-Dyson distribution. A convenient way to probe

level statistics is by computing the so-called $\langle r \rangle$ parameter [S19], defined as the average of level spacing ratios:

$$r_n = \frac{\min(s_n, s_{n-1})}{\max(s_n, s_{n-1})}. \quad (\text{S29})$$

For the Poisson statistics, we expect $\langle r \rangle \approx 0.39$, while $\langle r \rangle \approx 0.53$ for Wigner-Dyson. In Fig. S20 we show that $\langle r \rangle$ tends towards 0.53 as N increases, for all values of μ . In general, as μ becomes larger, the convergence is slower because the detuning approximately conserves the number of excitations. Beyond that, one can also notice two dips in $\langle r \rangle$ at $\mu = 0$ and $\mu \approx 1.6$, hinting that near these values PXP is close to another integrable model. For pure PXP this had been noted and previously investigated with various other perturbations [S20].

The full distribution of the s_n is shown in Fig. S21 for $\mu = 0, 1$, and 1.6829 for $N=32$ spins. In all cases, we see that the distribution resembles Wigner-Dyson, even though in the last case it is skewed towards zero.

In conclusion, for any finite value of μ , the PXP model is non-integrable and its level statistics follow the

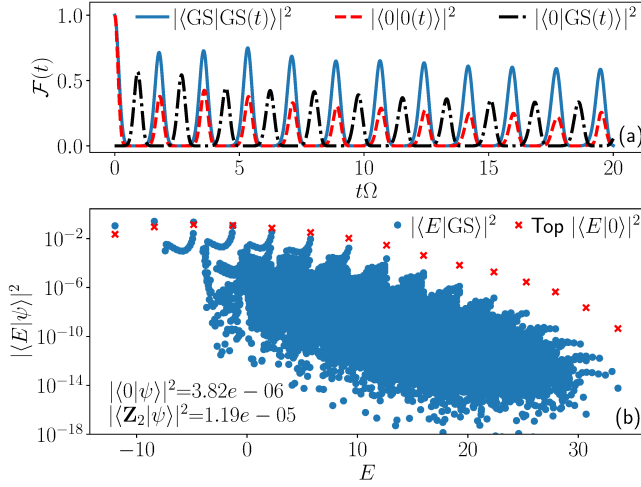


Figure S19. Emergence of many-body scarring by quenching the PXP model from $\mu_i = -0.76\Omega$ to $\mu_f = 1.6\Omega$ for $N = 32$ spins in the $k=0, p=1$ symmetry sector. The dynamics is very similar to that of the polarized state at the same μ_f , with the overlap between the two suggesting that state transfer happens between them. The overlap between these two states and the eigenstates of $\hat{H}(\mu_f)$ also shows similar tower structures.

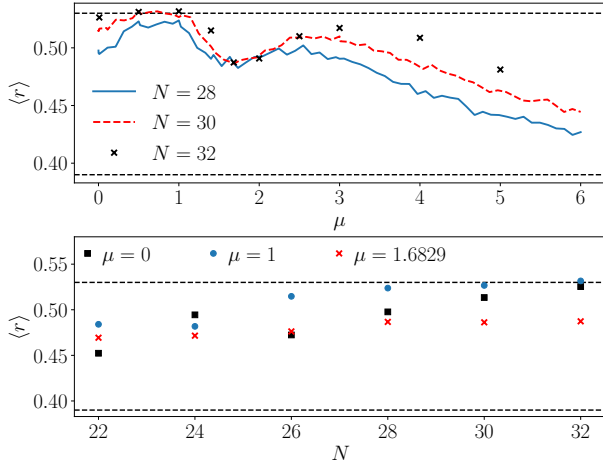


Figure S20. $\langle r \rangle$ for the PXP model with various system sizes N and detuning μ . For all values of μ shown, the spectral statistics flows towards Wigner-Dyson value, as the $\langle r \rangle$ parameter increases with system size. However the convergence is slower near $\mu = 0$, $\mu = 1.68$, and in general as μ becomes larger.

Wigner-Dyson distribution in a large enough system size. Interestingly, the level statistics suggests a proximity to an integrable model at the points where we find good revivals due to scars: at $\mu = 0$ for the Néel state and near $\mu = 1.68$ for the polarized state. These results are in accordance with the discrepancies observed between the diagonal and canonical ensembles in Fig. S16.

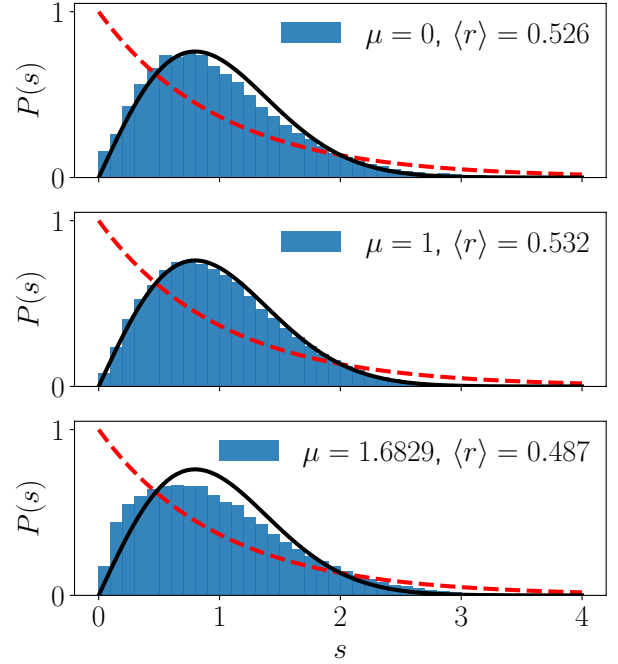


Figure S21. Distribution of the level spacings after spectrum unfolding for the PXP model with $N=32$. The solid black line corresponds to the Wigner-Dyson distribution and the dashed red line to Poisson. In all cases the distribution is close to Wigner-Dyson, even though for $\mu = 1.6829$ it is skewed towards $s = 0$.

SYSTEM-SIZE SCALING OF THE REVIVAL FIDELITY

An important question concerns the stability of revivals in the thermodynamic limit. In particular, due to the cost of non-linear optimization, the driving parameters were obtained in relatively small systems, therefore it needs to be checked whether the same parameters work as well in large systems. For the calculations in this section, we perform time evolution in large systems using the TEBD algorithm implemented in TenPy package [S9], as explained in Sec. .

Figs. S22 and S23 show the system size scaling of the first three revival peaks for different initial states, both with and without driving. The results were obtained from numerical simulations of the tilted Bose-Hubbard model, Eq. (S26), with open boundary conditions, $\Delta/J = 16$, and maximally 3 particles per site. This particle number limit is a reasonable assumption since the periodically driven interaction strength $U(t) = \Delta + U_0 + U_m \cos(\omega t)$ is large compared to the hopping amplitude J . In the case of global fidelity $F(t)$, we plot the so-called fidelity density $-\ln(F(nT))/L$, where T is the revival period and $n \in \{1, 2, 3\}$. The single-site fidelity $\mathcal{F}_{(1)}(t)$ is a local quantity, so it does not need to be rescaled by the system size L . We therefore simply

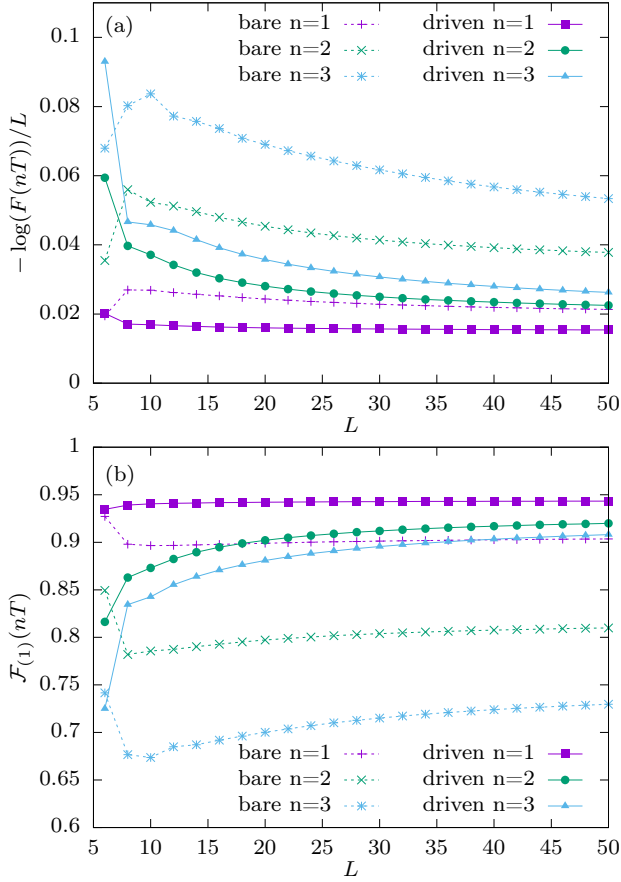


Figure S22. System size scaling of the first three revival peaks for the Néel state $|\mathbb{Z}_2\rangle = |2020\dots 20\rangle$. Driving parameters $\omega = 3.85$, $U_0 = 1.85$, $U_m = 3.71$. Dashed lines correspond to the bare case and the solid lines to the driven case. (a) Fidelity density. (b) Single-site fidelity.

plot the peak heights $\mathcal{F}_{(1)}(nT)$.

For the Néel state $2020\dots 20$, the fidelity density is expected to converge to a constant value in the limit of large L . This is consistent with our results in Fig. S22(a), where we plot the fidelity density after one, two and three driving periods. The driving parameters are the same for all system sizes, $\omega = 3.85$, $U_0 = 1.85$ and $U_m = 3.71$. Due to the minus sign in the definition, lower fidelity density corresponds to higher revival peaks and vice versa. As can be observed in Fig. S22(a), periodic driving leads to increased revivals over a broad range of system sizes and there is no indication that this will change for $L > 50$. The revivals are decaying with time, but the decay is significantly slower when the driving is turned on. We can thus conclude that periodic driving with these parameters both enhances and stabilises the revivals, even in relatively large systems.

The scaling of the single-site fidelity can be observed in Fig. S22(b). This experimentally measurable quantity represents a tight upper bound for the global fidelity when the system is initialized in a product state, see Sec-

tion . The results are similar to those for the global fidelity. In all cases, the revival heights are rapidly converging towards a constant value. Again, the revivals in driven systems are significantly higher than those without driving and the difference between them increases with time.

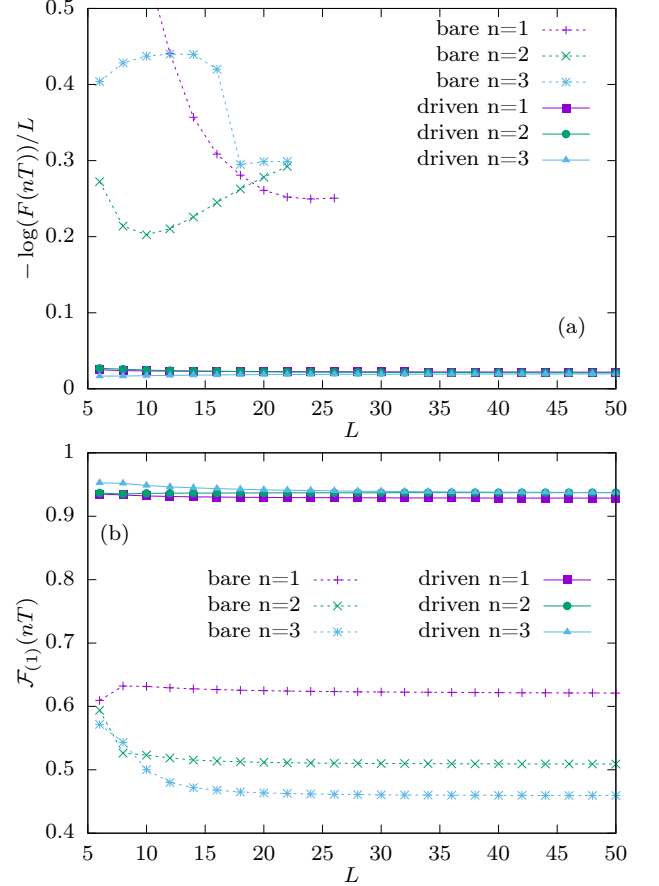


Figure S23. System size scaling of the first three revival peaks for the polarized state $|111\dots 111\rangle$. Driving parameters $\omega = 4.90$, $U_0 = -2.38$, $U_m = 1.54$. Dashed lines correspond to the bare case and the solid lines to the driven case. Data points are missing in cases where there are no local maxima. (a) Fidelity density. (b) Single-site fidelity.

The effects of periodic driving are even more striking with the polarized state $111\dots 111$ as the initial state, as shown in Fig. S23. There are no notable revivals in global fidelity when the driving is turned off. The dashed lines in Fig. S23(a) correspond to irregular minor local maxima which are present in smaller systems. Even these local maxima disappear with increasing system size, which explains why some data points are missing. In contrast, driving with parameters $\omega = 4.90$, $U_0 = -2.38$ and $U_m = 1.54$ produces very high revivals which do not decay, either with time or with system size. The single-site fidelity tells a similar story, see Fig. S23(b), however in this case there are revivals even in the absence of driving, consistent with dynamics of local observables in

Fig. S12(b).

Finally, we note that the Néel and polarized states are the only two initial product states for which we were able to find optimal driving parameters that lead to robust revivals at late times. This is true both for the tilted Bose-Hubbard model, Eq. (S26) in the $\Delta \approx U$ regime, and for the PXP model with a spatially uniform driving protocol. For other initial states, such as \mathbb{Z}_4 state with an excitation on every fourth site or, equivalently, 20112011...2011 in the tilted Bose-Hubbard model, it is possible to stabilize a small number of revivals at short times. In contrast to the Néel and polarized states, these revivals are found to decay quickly with time as well as with system size.

-
- [S1] I. Lesanovsky and H. Katsura, *Phys. Rev. A* **86**, 041601 (2012).
- [S2] P. Fendley, K. Sengupta, and S. Sachdev, *Phys. Rev. B* **69**, 075106 (2004).
- [S3] S. Sachdev, K. Sengupta, and S. M. Girvin, *Phys. Rev. B* **66**, 075128 (2002).
- [S4] K. Sengupta, “Phases and dynamics of ultracold bosons in a tilted optical lattice,” (2021), [arXiv:2109.02657](https://arxiv.org/abs/2109.02657) [[cond-mat.quant-gas](https://arxiv.org/abs/2109.02657)].
- [S5] C. J. Turner, A. A. Michailidis, D. A. Abanin, M. Serbyn, and Z. Papić, *Nature Physics* **14**, 745 (2018).
- [S6] C. J. Turner, A. A. Michailidis, D. A. Abanin, M. Serbyn, and Z. Papić, *Phys. Rev. B* **98**, 155134 (2018).
- [S7] S. Bravyi, D. P. DiVincenzo, and D. Loss, *Ann. Phys.* **326**, 2793 (2011).
- [S8] G. Vidal, *Phys. Rev. Lett.* **91**, 147902 (2003).
- [S9] J. Hauschild and F. Pollmann, *SciPost Phys. Lect. Notes*, **5** (2018), code available from <https://github.com/tenpy/tenpy>, [arXiv:1805.00055](https://arxiv.org/abs/1805.00055).
- [S10] J. C. Halimeh, R. Ott, I. P. McCulloch, B. Yang, and P. Hauke, *Phys. Rev. Research* **2**, 033361 (2020).
- [S11] F. M. Surace, P. P. Mazza, G. Giudici, A. Lerose, A. Gambassi, and M. Dalmonte, *Phys. Rev. X* **10**, 021041 (2020).
- [S12] D. Bluvstein, A. Omran, H. Levine, A. Keesling, G. Semeghini, S. Ebadi, T. T. Wang, A. A. Michailidis, N. Maskara, W. W. Ho, S. Choi, M. Serbyn, M. Greiner, V. Vuletić, and M. D. Lukin, *Science* **371**, 1355 (2021).
- [S13] N. Maskara, A. A. Michailidis, W. W. Ho, D. Bluvstein, S. Choi, M. D. Lukin, and M. Serbyn, *Phys. Rev. Lett.* **127**, 090602 (2021).
- [S14] H. Bernien, S. Schwartz, A. Keesling, H. Levine, A. Omran, H. Pichler, S. Choi, A. S. Zibrov, M. Endres, M. Greiner, V. Vuletić, and M. D. Lukin, *Nature* **551**, 579 (2017).
- [S15] B. Mukherjee, A. Sen, D. Sen, and K. Sengupta, *Phys. Rev. B* **102**, 075123 (2020).
- [S16] J. M. Deutsch, *Phys. Rev. A* **43**, 2046 (1991).
- [S17] M. Srednicki, *Phys. Rev. E* **50**, 888 (1994).
- [S18] Z. Yao, L. Pan, S. Liu, and H. Zhai, “Quantum many-body scars and quantum criticality,” (2021), [arXiv:2108.05113](https://arxiv.org/abs/2108.05113) [[cond-mat.quant-gas](https://arxiv.org/abs/2108.05113)].
- [S19] V. Oganesyan and D. A. Huse, *Phys. Rev. B* **75**, 155111 (2007).
- [S20] V. Khemani, C. R. Laumann, and A. Chandran, *Phys. Rev. B* **99**, 161101 (2019).